

## Origin of magnetovolume effect in a cobaltite

Ping Miao <sup>1,\*</sup>, Zhijian Tan,<sup>1,2</sup> Sanghyun Lee,<sup>1</sup> Yoshihisa Ishikawa,<sup>1</sup> Shuki Torii,<sup>1</sup> Masao Yonemura,<sup>1,2</sup> Akihiro Koda,<sup>1,2</sup> Kazuki Komatsu,<sup>3</sup> Shinichi Machida,<sup>4</sup> Asami Sano-Furukawa,<sup>5</sup> Takanori Hattori,<sup>5</sup> Xiaohuan Lin,<sup>6,7</sup> Kuo Li,<sup>6</sup> Takashi Mochiku,<sup>8</sup> Ryosuke Kikuchi,<sup>9</sup> Chizuru Kawashima,<sup>9</sup> Hiroki Takahashi,<sup>9</sup> Qingzhen Huang,<sup>10</sup> Shinichi Itoh <sup>1,2</sup>, Ryosuke Kadono <sup>1,2</sup>, Yingxia Wang,<sup>7</sup> Feng Pan,<sup>11</sup> Kunihiko Yamauchi <sup>12,†</sup> and Takashi Kamiyama<sup>1,2,‡</sup>

<sup>1</sup>*Institute of Materials Structure Science, High Energy Accelerator Research Organization (KEK), Tokai 319-1106, Japan*

<sup>2</sup>*Sokendai (The Graduate University for Advanced Studies), Tokai 319-1106, Japan*

<sup>3</sup>*Geochemical Research Center, Graduate School of Science, The University of Tokyo, Tokyo 113-0033, Japan*

<sup>4</sup>*Neutron Science and Technology Center, CROSS, Tokai, Ibaraki 319-1106, Japan*

<sup>5</sup>*J-PARC Center, Japan Atomic Energy Agency (JAEA), Tokai, Ibaraki 319-1195, Japan*

<sup>6</sup>*Center for High Pressure Science and Technology Advanced Research, Beijing, 100094, China*

<sup>7</sup>*College of Chemistry and Molecular Engineering, Peking University, Beijing 100871, China*

<sup>8</sup>*National Institute for Materials Science (NIMS), Tsukuba, Ibaraki 305-0047, Japan*

<sup>9</sup>*Department of Physics, College of Humanities and Sciences, Nihon University, Tokyo, 156-8550, Japan*

<sup>10</sup>*NIST Center for Neutron Research, National Institute of Standards and Technology, 100 Bureau Drive, Gaithersburg, Maryland 20899, USA*

<sup>11</sup>*School of Advanced Materials, Peking University, Shenzhen Graduate School, Shenzhen 518055, China*

<sup>12</sup>*ISIR-SANKEN, Osaka University, Ibaraki, Osaka 567-0047, Japan*



(Received 25 September 2018; revised 11 January 2021; accepted 8 February 2021; published 8 March 2021)

The layered perovskite  $\text{PrBaCo}_2\text{O}_{5.5+x}$  demonstrates a strong negative thermal expansion (NTE) which holds potential for being fabricated into composites with zero thermal expansion. The NTE was found to be intimately associated with the spontaneous magnetic ordering, known as magnetovolume effect (MVE). Here we report with compelling evidence that the continuouslike MVE in  $\text{PrBaCo}_2\text{O}_{5.5+x}$  is intrinsically of discontinuous character, originating from a magnetoelectric transition from an antiferromagnetic insulating large-volume (AFILV) phase to a ferromagnetic less-insulating small-volume (FLISV) phase. Furthermore, the magnetoelectric effect (ME) shows high sensitivity to multiple external stimuli such as temperature, carrier doping, hydrostatic pressure, magnetic field, etc. In contrast to the well-known ME such as colossal magnetoresistance and multiferroic effect which involve symmetry breaking of crystal structure, the ME in the cobaltite is purely isostructural. Our discovery provides a pathway to realizing the ME as well as the NTE, which may find applications in new techniques.

DOI: [10.1103/PhysRevB.103.094302](https://doi.org/10.1103/PhysRevB.103.094302)

### I. INTRODUCTION

The “Invar effect” originates from the discovery by Guillaume [1] in 1897 that the  $\text{Fe}_{65}\text{Ni}_{35}$  alloy undergoes almost zero thermal expansion in a wide range of temperature. Since then, various alloys with very low thermal expansion coefficient, known as Invar alloys, have been developed and applied to fields where dimensional stability is required, ranging from precision instruments such as telescopes, standard rulers, timing devices, etc., to large structural components like railroad tracks, bridges, liquefied natural gas containers, and so on [2]. It is generally agreed upon that the normal positive thermal expansion from phonons in Invar alloys is compensated by a negative contribution arising from spontaneous magnetic ordering, which is known as the magnetovolume effect (MVE) [2,3]. Although diverse theoretical models from different perspectives have been proposed to explain the profound MVE [4–17], there is still no consensus on the microscopic origin.

One of the difficulties in experimentally justifying the theories lies in the fact that the alloys contain chemical inhomogeneities that hinder the detection of intrinsic electromagnetic inhomogeneities.

Oxides have been proved to be chemically homogeneous platforms for investigating electromagnetic phase separations. For example, multiple experimental evidences have demonstrated the coexistence of the antiferromagnetic Mott-insulating phase and superconducting phase in cuprates [18], as well as the competition between the antiferromagnetic charge-ordered/orbital-ordered insulating phase and ferromagnetic charge-disordered/orbital-disordered metallic phase in colossal magnetoresistive (CMR) manganites [19,20]. Therefore, we investigated the MVE in a cobaltite with layered perovskite structure,  $\text{PrBaCo}_2\text{O}_{5.5+x}$  with hole doping level  $0 \leq x \leq 0.41$ . The compound crystallizes into the  $Pm\bar{m}m(a_p \times 2a_p \times 2a_p)$  structure at hole doping level  $0.06 < x \leq 0.41$  and into the  $Pmma(2a_p \times 2a_p \times 2a_p)$  structure at  $x \leq 0.06$  [21,22]. The cobaltite was first reported to exhibit continuouslike MVE at about  $x = 0.25$  [23]. The ground state for  $x \leq 0.24$  is characterized as a long-ranged ordered antiferromagnetic structure, which transforms into a ferromagnetic one for  $x \geq 0.26$  [21]. As shown in Fig. 1(a), upon

\*miao@post.kek.jp

†kunihiko@sanken.osaka-u.ac.jp

‡takashi.kamiyama@kek.jp

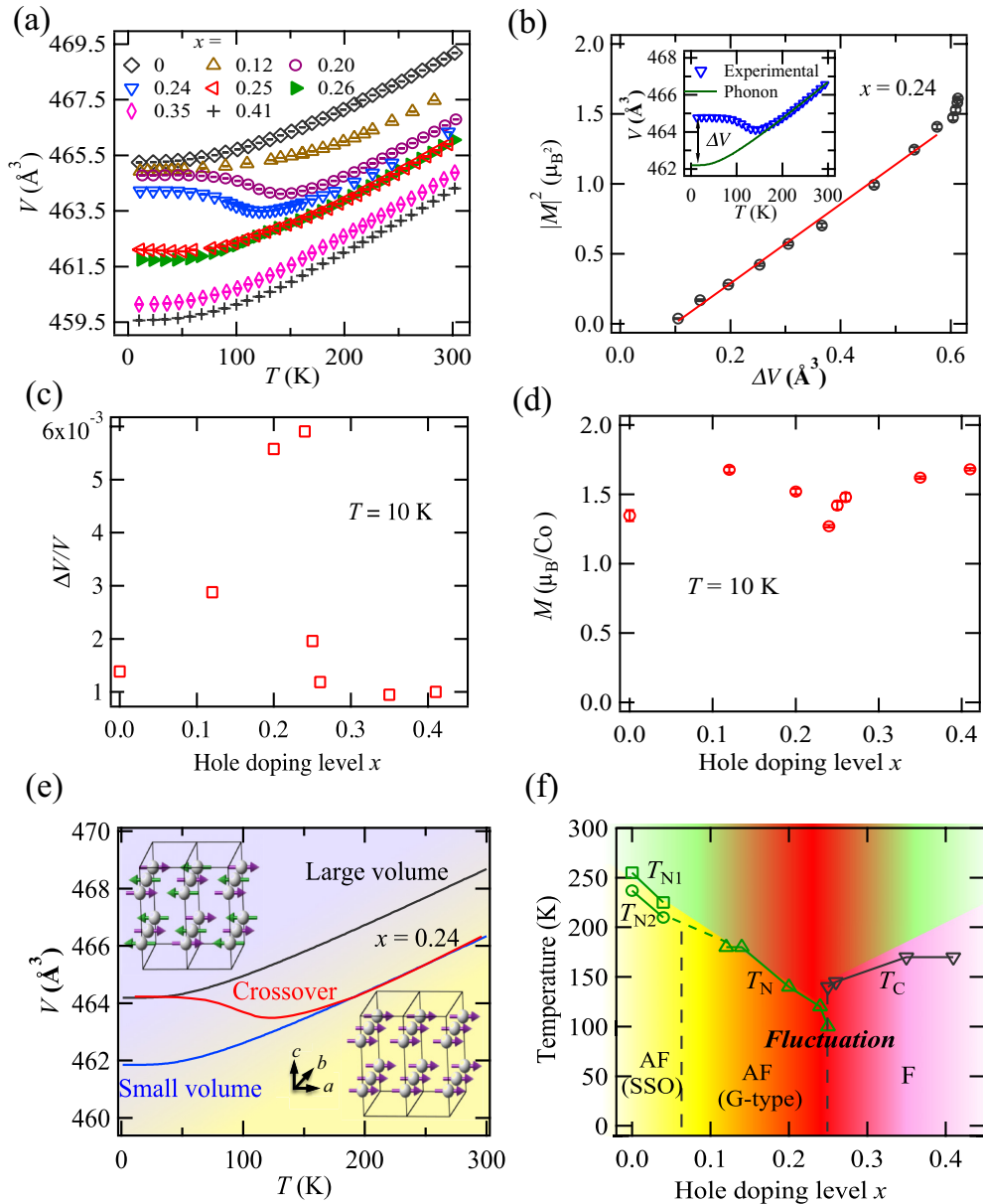


FIG. 1. Unit cell volume (a), magnetovolume (b),(c), Co-ion magnetic moments (d), transition model (e), and phase diagram (f) of  $\text{PrBaCo}_2\text{O}_{5.5+x}$ . All the results are derived from analysis of high-resolution NPD data. (a) Volume of sub unit cell ( $2a_p \times 2a_p \times 2a_p$ ) as a function of temperature for various hole-doping fraction  $x$  which shows that anomalous thermal expansion is enhanced with increasing  $x$  until maximum at  $x = 0.24$  and drops with further hole doping. (b) Square of magnetic moment  $|M|^2$  as a function of volumetric order parameter  $\Delta V$  for  $x = 0.24$ .  $M$  is determined from Rietveld refinement using a G-type antiferromagnetic structure model.  $\Delta V$  is extracted by subtracting the phonon contribution, which is calculated on the basis of the Debye-Grüneisen model as shown in the inset. The details of the calculations are described in the Appendix. The solid red line is the linear fit to the data. (c) Spontaneous magnetovolume contribution at 10 K as a function of hole-doping fraction  $x$ , derived in the same ways as that for  $x = 0.24$ . (d) Magnetic moment of single Co ion at  $T = 10$  K as a function of hole doping level  $x$ , which is determined from Rietveld refinement. The residual values  $R_{wp}$  is both below 10% and  $R_M$  below 20%. For the spin-state ordered (SSO) phase at  $x = 0$ , where different crystallographic sites of Co bear different magnetic moments, the magnetic moment is averaged over all Co sites. For the coexisting long-range ordered ferromagnetic and antiferromagnetic phases at  $x = 0.25$ , the magnetic moment is averaged over both phases. (e) The magneto-electric transition model for NTE of  $x = 0.24$ , i.e., the transition from an AFILV phase with antiferromagnetic (G-type) structure of Co spins (the upper-left drawing) to a FLISV phase with the ferromagnetic structure (the lower-right drawing). (f) Phase diagram for  $\text{PrBaCo}_2\text{O}_{5.5+x}$ , summarized from our previous [21] and present NPD experiments. AF(SSO), AF(G-type), and F denote the antiferromagnetic (spin-state ordering), antiferromagnetic (G-type), and ferromagnetic states, respectively.  $T_{N1}$  (green squares) and  $T_{N2}$  (green circles),  $T_N$  (green triangles), and  $T_C$  (black triangles) represent the transition temperatures for these long-range ordered magnetic structures. Strong phase fluctuations occur near the boundary between F and AF phases, as highlighted by the red shadows.

hole doping anomalous thermal expansion (ATE) occurs from  $x = 0.12$  and evolves into negative thermal expansion (NTE) at  $x = 0.20$ . The NTE reaches extreme at  $x = 0.24$  and promptly returns to normal positive thermal expansion (PTE) at  $x > 0.26$ . Figure 1(b) shows that the volumetric order parameter  $\Delta V$  is linearly coupled with the square of magnetic moment  $M$  at  $x = 0.24$ , evidencing the MVE. The  $M$  arises continuously from zero so that the MVE looks like the second-order (continuous) phase transition. In analogy with the Invar alloys, the doping dependence of MVE also shows a peak centered at hole doping level  $x \approx 0.24$  [Fig. 1(c)] [3,21]. From this perspective, our study on  $\text{PrBaCo}_2\text{O}_{5.5+x}$  may shed light on the controversial origin for MVE in Invar alloys.

The experimental evidences and theoretical calculations reported here reveal that the ground state near the boundary in the phase diagram, at  $x \approx 0.24$ , has two separate energy minima, i.e., an antiferromagnetic insulating large-volume (AFILV) phase and a ferromagnetic less-insulating small-volume (FLISV) phase. As shown in Fig. 1(e), both phases undergo normal positive thermal expansion at finite temperatures, following the Debye-Gruneisen model (see the Appendix) that accounts for the phonon-induced thermal expansion, and the NTE comes from temperature-induced transition from AFILV phase to FLISV phase.

The magnetoelectric transition is intimately connected with strong phase fluctuations between the AFILV and FLISV phases near the boundary [Fig. 1(f)], where the two phases intensely compete with each other. As a result, moderate external stimuli in addition to temperature ( $T$ ), such as carrier doping ( $x$ ), hydrostatic pressure ( $P$ ), magnetic field ( $H$ ), etc., can also induce the conversion between the two phases, triggering giant multiple responses. To be noted, there is no symmetry breaking of the crystal structure in the process of the AFILV-FLISV phase transition, which is different from the well-known magnetoelectric effect (ME) in bulk materials like CMR and multiferroic effect. As we know, the charge/orbital order in the insulating phase melts upon transitioning into the metallic phase in CMR materials [19,24] while the inversion symmetry breaks so as to induce ferroelectricity in multiferroics [20,25]. The isostructural AFILV-FLISV phase transition in the cobaltite opens another way of generating ME in bulk materials, which holds substantial potential for new industrial applications.

## II. METHOD

### A. Sample preparation

$\text{PrBaCo}_2\text{O}_{5.5+x}$  polycrystalline samples were synthesized by the solid-state reaction method with a combined EDTA-citrate complex sol-gel process [21,22]. Solutions of praseodymium nitrate were prepared by dissolving high-purity oxide  $\text{Pr}_6\text{O}_{11}$  into dilute nitric acids. Solutions of barium and cobalt nitrates were prepared by dissolved the nitrates in deionized water, respectively. Their precise concentrations were determined by titration with EDTA. The solutions of stoichiometric molar ratios of metal ions were mixed with adding some citric acid. The mixture was heated and stirred at  $90^\circ\text{C}$  until sufficient water had evaporated and a dry resin formed. The resin was then calcinated in air at  $300^\circ\text{C}$  for two hours and at  $500^\circ\text{C}$  for five hours to remove

the organic residues. The resultant powders were sintered in an electrical box furnace at  $1200^\circ\text{C}$  for 48 hours and slowly cooled down ( $\sim 2^\circ\text{C}/\text{min}$ ) to room temperature. High crystallinity of the as-synthesized samples was identified by high-resolution neutron powder diffraction experiments.

The oxygen content was controlled by annealing the as-prepared samples at various temperatures and under different gas atmospheres for 24 hours, followed by a slow cooling down ( $\sim 2^\circ\text{C}/\text{min}$ ) process. The fraction  $x$  was determined by both iodometric titration and Rietveld refinement (occupancy parameters) on neutron powder diffraction data, with the results agreeing with each other within the error of  $\sim 0.02$ . The  $x$  value of as-synthesized sample was determined to be 0.20.  $x = 0$  and  $x = 0.12$  were obtained by annealing under pure nitrogen gas-flow atmosphere at  $515^\circ\text{C}$  and  $350^\circ\text{C}$ , respectively.  $x = 0.24$ ,  $x = 0.25$ , and  $x = 0.26$  were obtained by annealing in the air at  $1050^\circ\text{C}$ ,  $1025^\circ\text{C}$ , and  $1000^\circ\text{C}$ , respectively.  $x = 0.35$  and  $x = 0.41$  were obtained by annealing in an autoclave with pure high-pressure (5 MPa) oxygen gas at  $350^\circ\text{C}$  and  $300^\circ\text{C}$ , respectively. To be noted, the three samples of  $x = 0.24$ ,  $x = 0.25$ , and  $x = 0.26$  are in principle indistinguishable in the light of the error of  $\sim 0.02$ . Our neutron powder diffraction experiments show that the unit cell volumes at room temperature and the magnetic ground state changes systematically from  $x = 0.24$  to  $x = 0.26$ . At  $x = 0.24$ , the unit cell volume is the largest among the three and long-range AF ordering occurs at ground state. At  $x = 0.25$ , the unit cell size is intermediate and the magnetic ground state consists of both long-range AF and F ordering. At  $x = 0.26$ , the unit cell volume size is smallest and long-range F ordering occurs at ground state.

### B. Neutron powder diffraction (NPD)

The high-resolution NPD measurements were performed using SuperHRPD [26] at Japan Proton Accelerator Research Complex (J-PARC). The averaged resolution for the backscattering detector complex ( $155^\circ < 2\theta < 175^\circ$ ) is  $\frac{\Delta d}{d} = 0.09\%$ . The samples were mounted in a top-loading closed cycle refrigerator with base temperature  $T = 10$  K.

The magnetic-field NPD measurements were also carried out at SuperHRPD by implementing the Oxford superconducting magnet with a liquid helium cryostat. The superconducting magnet is in the form of split pairs with magnetic field vector in the vertical plane of the cryostat. The sample was mounted through the top-loading access along the magnetic field direction. The magnetic field can be tuned from 0 up to 14 T at any temperature between 1.5 K and 300 K.

The high-pressure NPD measurements were performed using PLANET [27] at J-PARC. The Mito system [28] equipped with anvils made of  $\text{ZrO}_2$  was implemented for high-pressure and low-temperature controlling, which can reach highest pressure  $P = 5$  GPa and base temperature  $T = 77$  K. The sample was loaded with a pressure-transmitting medium of deuterated glycerol in a pair of encapsulating TiZr gaskets fitted in a tapered Al ring. The pressure is determined from lattice parameter of Pb based on the EOS [29]. The temperature is measured by two Pt resistance temperature sensors attached to the body of the press. The sample was cooled to 80 K before applying pressure up to  $P = 1.4$  GPa.

We conducted the symmetry analysis based on the representation theory using the software suits, BASIREPS [30] and SARAH [31], and carried out the Rietveld refinement with the software suites, Z-RIETVELD [32,33] and FULLPROF [30].

### C. Muon spin relaxation ( $\mu$ SR)

Time-differential muon ( $\mu^+$ ) spin relaxation was measured using S-line at J-PARC. The polycrystalline  $\text{PrBaCo}_2\text{O}_{5.5+x}$  samples were pressed into a pellet of 5 mm thickness and 25 mm diameter and mounted in a helium-flow cryostat with base temperature  $T = 4$  K. The measurements were conducted under the longitudinal magnetic field up to  $H = 0.4$  T in the parallel direction with respect to the initial  $\mu^+$  spin polarization. The data were analyzed using the software suite, *musrfit* [34].

### D. Magnetization and resistivity

The isothermal dc-magnetization ( $M$ - $H$  curve) was measured by the Quantum Design physical property measurement system (PPMS) at the Cross-Tokai user laboratories. The resistivity under magnetic field were also measured using a standard dc four-probe method on the PPMS. The high-pressure dc-magnetization ( $M$ - $T$  curve) was measured up to  $P = 1.2$  GPa using the piston-cylinder device implemented on the superconducting quantum interference device (SQUID) magnetometer (MPMS) at Department of Physics, Nihon University. Machine oil was used as the pressure-transmitting medium. The magnetization of the high-pressure device was subtracted after the measurement.

### E. Density-functional-theory (DFT) calculations

DFT calculations were performed using the VASP code [35] with generalized gradient approximation (GGA) potential. In order to account for correlation effects of  $3d$  electrons, we employed the Heyd-Scuseria-Ernzerhof (HSE) screened hybrid functional method [36], which mixes the exact non-local Fock exchange and the density-functional parametrized exchange. The HSE is known to improve the evaluation of band gap energy and the structural distortion, with respect to GGA+ $U$  approaches [37]. Both the atomic coordinates and the lattice parameters were fully optimized starting with the experimental values while spin-orbit interaction is not taken into account. It has been reported that samples of  $0.06 < x \leq 0.41$  crystallize into the  $Pmmm$  of ( $a_p \times 2a_p \times 2a_p$ ) structure [21,22], which features disorder of the oxygen vacancy. Since DFT calculations cannot account for the structure disordering, we adopted a supercell [with the space group orthorhombic  $Pmma$  of ( $2a_p \times 2a_p \times 2a_p$ )] containing four f.u. of  $\text{PrBaCo}_2\text{O}_{5.5+x}$  ( $x = 0.25$ ) is built to take into account the ordering patterns of oxygen-vacancy and spin/charge/orbital states at eight Co sites as shown in Fig. 11(a).

The average valence of Co ion at  $x = 0.25$  is 3.25 so that the eight Co ions in the super cell may show the charge ordering patterns with six trivalent and two quadrivalent ions. Besides, the Co ion may take three spin states in terms of the three configurations of  $3d$  electrons. In the case of the trivalent ion, it has low-spin (LS,  $t_{2g}^6 e_g^0$ ,  $S = 0$ ), intermediate-spin (IS,  $t_{2g}^5 e_g^1$ ,  $S = 1$ ), and high-spin (HS,  $t_{2g}^4 e_g^2$ ,  $S = 2$ ) states. This

makes the combination number with eight Co charge/spin states enormous in the calculation. To solve the problem, only the spin direction was imposed on each Co  $3d$  state by tuning the density matrix [38] while the orbital and charge states were automatically determined when the crystal structure is relaxed. As a result, an antiferromagnetic insulating state was stabilized in an HSE calculation with  $E_{\text{gap}} = 0.2$  eV. The ferromagnetic configuration with metallic ground state is also stabilized in a similar procedure.

## III. RESULTS

At  $x = 0.24$ , where the robust NTE and MVE is observed, the ground-state magnetic structure is a G-type antiferromagnetic structure [22] [see the inset of Fig. 1(e)]. To identify the existence of the ferromagnetic state with smaller volume and slightly higher energy than in the AF state, we investigated simultaneously the nuclear and magnetic structures by neutron powder diffraction (NPD) under hydrostatic pressure and magnetic field.

### A. NPD

Figure 2 shows the results of high-pressure NPD on the  $x = 0.24$  sample. Melting of AF order is evidenced by the complete suppression of magnetic reflection  $\frac{1}{2}11$  from the AF structure at  $P = 0.8$  GPa,  $T = 80$  K [Fig. 2(a)]. The formation of F order is indicated by the increase in integrated intensity of 002, 100, and 020 [Fig. 2(b)]. The comparison of the pressure dependence of integrated intensity between reflection 111 [Fig. 3(b)] of Pb used for pressure calibration and reflection 002 [Fig. 2(c)] of  $\text{PrBaCo}_2\text{O}_{5.5+x}$  ( $x = 0.24$ ), unambiguously reveals that the F reflection grows on top of the reflection 002 in  $x = 0.24$ . Simultaneously, the unit cell volume shrinks by 0.9% under the same pressure without any symmetry breaking of nuclear crystal structure [Fig. 2(f)]. These results lead to the conclusion that the antiferromagnetic large-volume phase transforms to the ferromagnetic small volume phase in the presence of hydrostatic pressure. The pressure dependence of integrated intensity [Fig. 2(c)] suggests that the transition initiates from below 0.4 GPa and completes at 0.8 GPa, in broad agreement with results of hydrostatic-pressure magnetization measurement that indicates the onset and end of the transition being 0.13 GPa and 1.12 GPa, respectively [Fig. 3(f)].

In contrast to the NTE under ambient pressure, the unit cell volume of ferromagnetic small-volume phase at 1.4 GPa exhibits positive thermal expansion [Fig. 2(d)], reminiscent of the same behavior in overdoped samples [e.g.,  $x = 0.41$  in Fig. 1(a)], which has been well described by the Debye-Gruneisen model and shows negligible MVE [21]. Both results corroborate that the pure ferromagnetic small volume phase exhibits positive thermal expansion. Also, the thermal expansion in the pure antiferromagnetic large-volume phase is assumed to be positive in light of the positive thermal expansion behavior in underdoped samples [e.g.,  $x = 0$  in Fig. 1(a)]. Consequently, the anomalous NTE as well as MVE at  $x = 0.24$  can be attributed to the transition from antiferromagnetic large-volume phase to ferromagnetic small-volume phase [Fig. 1(e)].

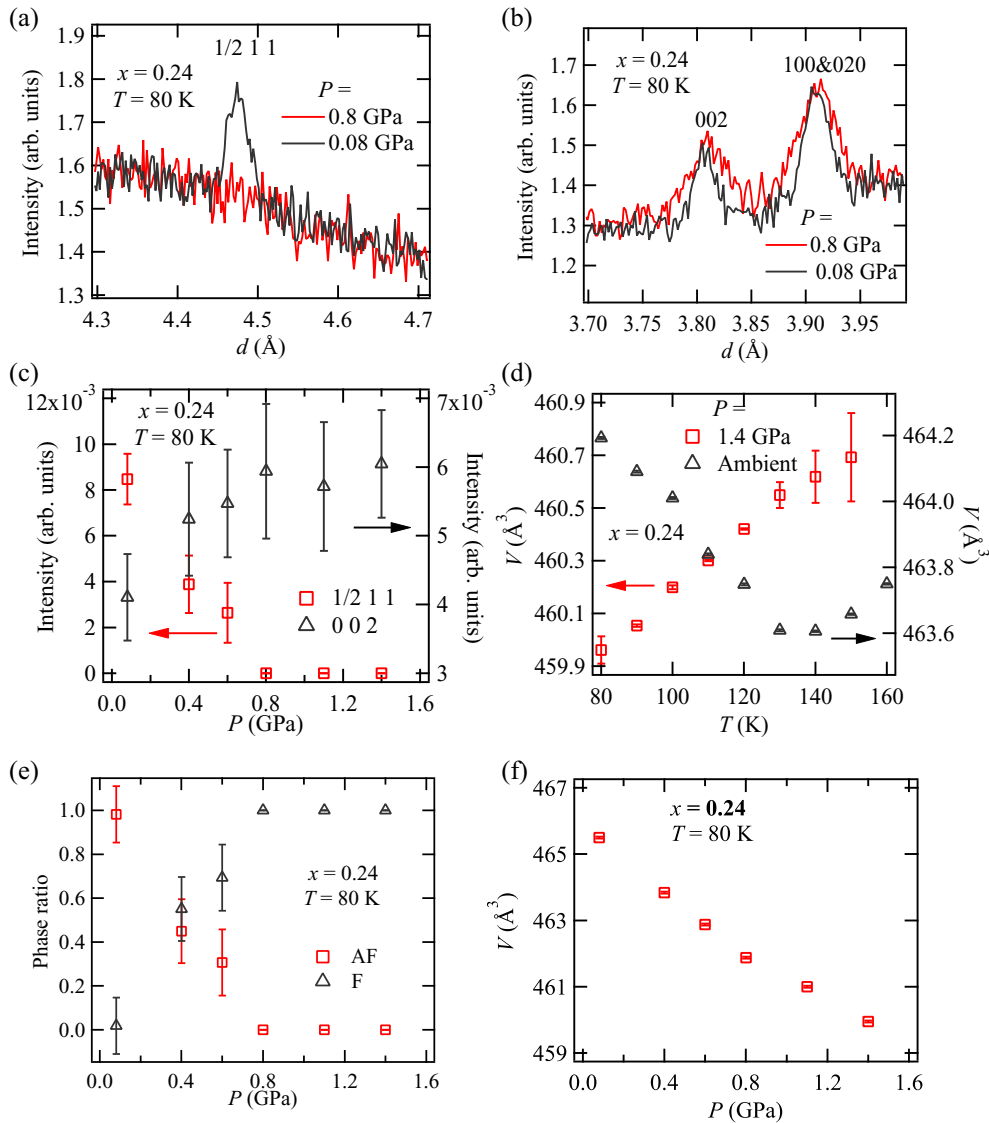


FIG. 2. Hydrostatic-pressure NPD on  $\text{PrBaCo}_2\text{O}_{5.5+x}$  ( $x = 0.24$ ). All the indices of reflections are given under the framework of nuclear unit cell ( $a_p \times 2a_p \times 2a_p$ ). There is no indication of symmetry breaking of the crystal structure under hydrostatic pressure up to  $P = 2.3$  GPa. (a),(b) Diffraction profiles showing antiferromagnetic (a) and ferromagnetic (b) peaks under ambient pressure and 0.8 GPa at 80 K. In the presence of hydrostatic pressure, the antiferromagnetic reflection  $\frac{1}{2}11$  is fully suppressed while the ferromagnetic reflections are identified from the increase in integrated intensity of reflections 002, 100, and 020, indicating the pressure-induced antiferromagnetic-ferromagnetic transition. (c) Integrated intensity of the magnetic reflections  $\frac{1}{2}11$  and 002 as a function of pressure at 80 K, suggesting the antiferromagnetic-ferromagnetic transition starts from below 0.4 GPa and completes at 0.8 GPa. (d) Volume of sub unit cell ( $2a_p \times 2a_p \times 2a_p$ ), obtained from Rietveld refinement, as a function of temperature under ambient pressure and 1.4 GPa, showing the NTE under ambient pressure disappears at high pressure (in the pure F phase). Between 80 to 150 K, the pressure varies from 1.38 GPa to 1.45 GPa. Assuming linear compressibility, the error of volume was estimated by  $\sigma = \frac{1.55\%}{2.3 \text{ GPa}} \times [P(T) - 1.38 \text{ GPa}] \times 460 \text{ \AA}^3$ , where the volume decreases by 1.55% at 2.3 GPa based on the diffraction experiment. (e) Phase fraction for ferromagnetic (F) and antiferromagnetic (AF) phases, obtained from integrated intensity as shown in panel (c), as a function of hydrostatic pressure at 80 K of  $x = 0.24$ . (f) Volume of sub unit cell ( $2a_p \times 2a_p \times 2a_p$ ) obtained from Rietveld refinement, as a function of hydrostatic pressure at 80 K of the  $x = 0.24$  sample.

The F peaks become broader upon applying pressure, which is partially due to a nonuniform distribution of pressure in the sample, as confirmed from the peak broadening of Pb. The Pb Bragg peak 111 becomes much broader with increasing the hydrostatic pressure [see Fig. 3(a)], indicating that lattice inhomogeneities are induced by a nonuniform distribution of pressure in the sample. The integrated intensity of Pb peak 111 shows independence on pressure [see Fig. 3(b)], corroborating that the peak broadening of Pb in Fig. 3(a) arises

from the pressure-induced lattice inhomogeneities. As the pressure increases, the F peaks become even broader than the Pb peaks [see Figs. 3(c) and 3(d)], indicating that part of peak broadening in F peaks is inherent to the samples itself. Since the peak broadening does not arise from symmetry breaking [see Fig. 2(f)], it might arise from the residual microstrain.

Analogous to hydrostatic pressure, magnetic field can also trigger the transition from antiferromagnetic large-volume phase to ferromagnetic small-volume phase at  $x = 0.24$ . As

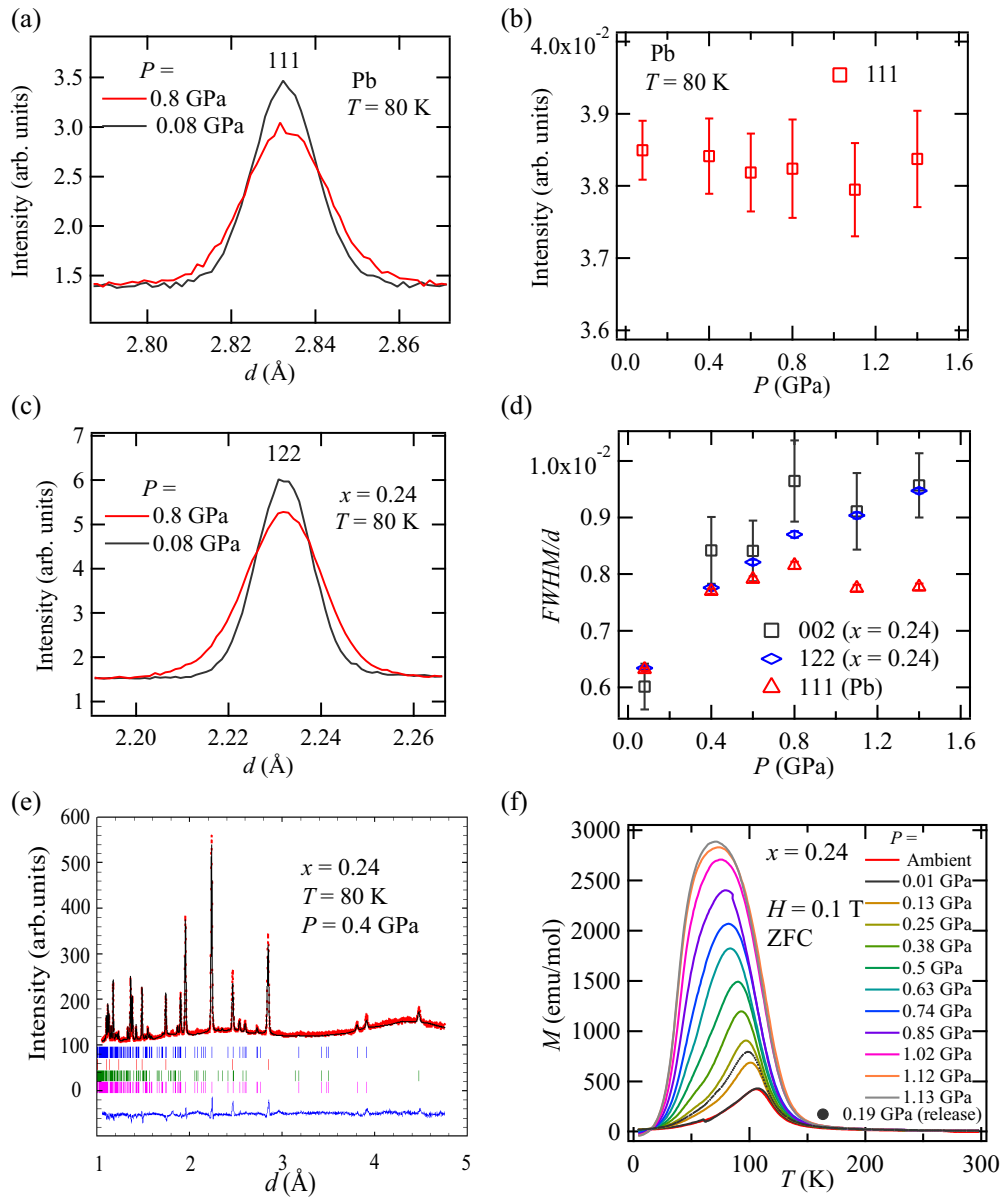


FIG. 3. High-pressure NPD (a),(b) for Pb, high-pressure NPD (c)–(e), and magnetization (f) for  $\text{PrBaCo}_2\text{O}_{5.5+x}$  ( $x = 0.24$ ). (a) Diffraction profiles of reflection 111 of Pb, which was used for pressure calibration, under 0.08 GPa and 0.8 GPa at 80 K. (b) Integrated intensity of the reflection 111 of Pb as a function of pressure at 80 K. (c) Diffraction profiles of reflection 122 of  $x = 0.24$ , under 0.08 GPa and 0.8 GPa at 80 K. (d) Full width at half maximum (FWHM) over  $d$ -spacing  $\frac{\text{FWHM}}{d}$  (relative peak width) of Bragg reflections (002 and 122 of  $x = 0.24$ , and 111 of Pb) as a function of pressure. The FWHMs are all derived from the Gaussian fitting to the NPD profiles. (e) Rietveld refinement on the data at  $T = 80$  K and  $P = 0.4$  GPa using the model of double phases (AFILV and FLISV). The F and AF structure models are shown in Fig. 1(e). Experimental data points are shown by red dots, and the black line through them is the fit by Rietveld analysis. Since the peaks of high-pressure NPD are too broad to identify the peak splitting from coexistence of the AFILV phase and the FLISV phase, the nuclear structures approximate to the same one as shown by the blue bars. The green bars denote the indices from antiferromagnetic structure, and magenta bars represent those of the ferromagnetic structure. The red bars indicate the nuclear structure of Pb. The blue line shows the difference between experiment and calculation. The residual value  $R_{wp}$  is 16.30% and  $R_M$  is 38.4%. (f) Molar magnetization as a function of temperature (M-T curve) measured under magnetic field of 0.1 T through zero-field cooling (ZFC) processes for various hydrostatic pressures. The M-T curves at different pressures were measured in the direction of increasing pressure except for that at 0.19 GPa.

shown in Figs. 4(a) and 4(b), upon applying the magnetic field of 14 T at 60 K, the antiferromagnetic reflection  $\frac{1}{2}11$  is significantly suppressed while the ferromagnetic reflections grow on top of the nuclear reflections 022, 102, and 120. From the temperature dependence of integrated intensity [Fig. 4(c)], we can see  $\frac{1}{2}11$  fully vanishes under the 14 T field at higher

temperatures such as 100 K and 110 K, whereas the F reflections initiate from 150 K upon cooling, coincident with the onset of deviation of unit cell volume from that under zero field as shown in Fig. 4(d). Therefore, the contraction of the unit cell is intimately associated with the change of magnetic structure, suggesting a field induced transition from

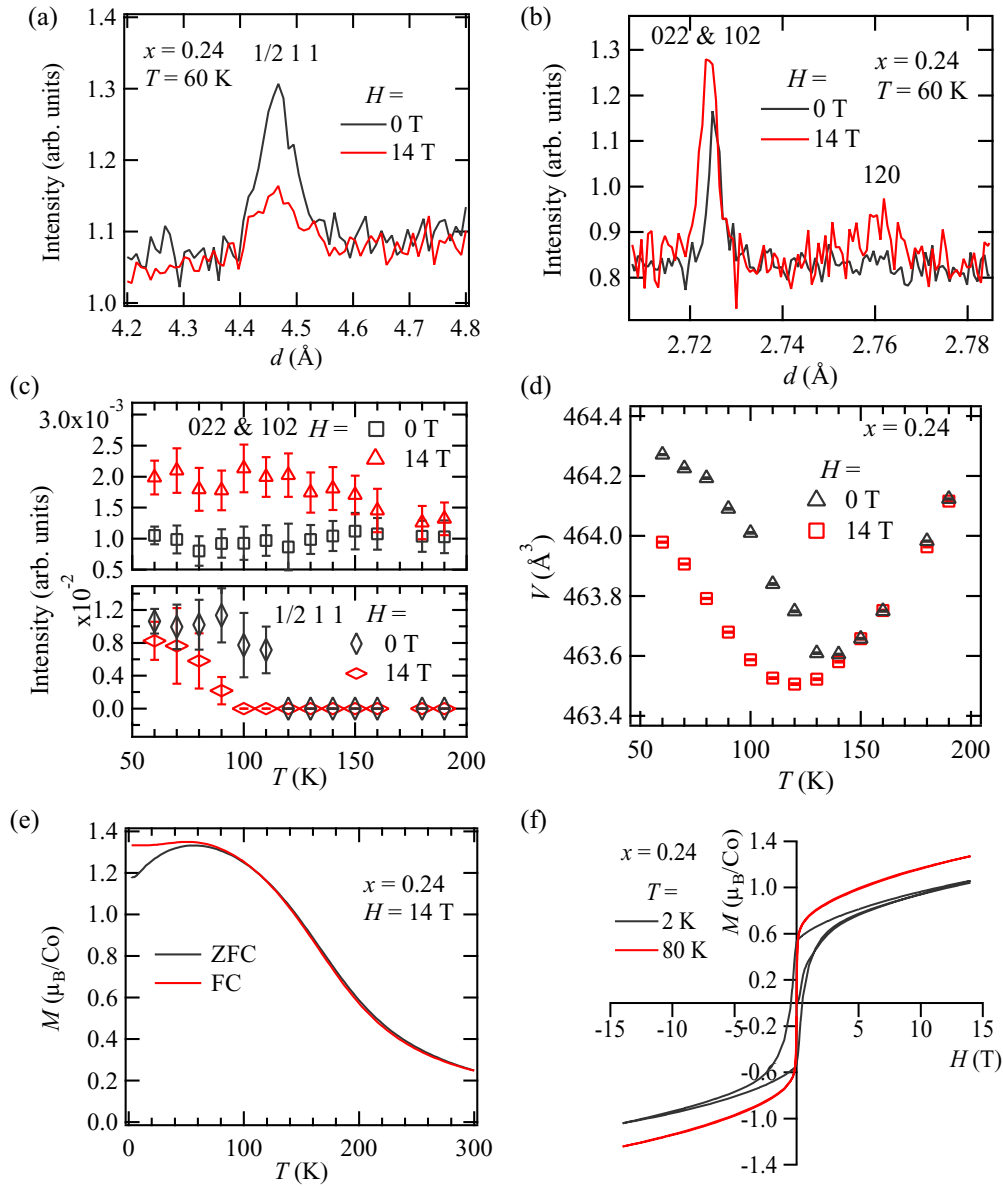


FIG. 4. Magnetic-field NPD (a)–(d) and DC magnetization (e),(f) on  $\text{PrBaCo}_2\text{O}_{5.5+x}$  ( $x = 0.24$ ). All the indices of reflections are given under the framework of nuclear unit cell ( $a_p \times 2a_p \times 2a_p$ ). No sign of symmetry breaking of nuclear crystal structure was observed under magnetic field up to 14 T. (a),(b) Diffraction profiles showing antiferromagnetic (a) and ferromagnetic (b) peaks under zero field and 14 T at 60 K. The antiferromagnetic reflection  $\frac{1}{2}11$  is suppressed while the ferromagnetic intensity grows on top of nuclear reflections 022, 102, and 120 by applying magnetic field, indicating a field-induced antiferromagnetic-ferromagnetic transition. (c) Integrated intensity of the magnetic reflections 022 and 102 (upper panel) and  $\frac{1}{2}11$  (lower panel) as a function of temperature under zero field and 14 T, respectively, showing that the magnetic field induces ferromagnetic ordering from 150 K while suppressing antiferromagnetic ordering from 120 K upon cooling. (d) Volume of sub unit cell ( $2a_p \times 2a_p \times 2a_p$ ), obtained from Rietveld refinement, as a function of temperature under zero field and 14 T, showing the unit cell significantly contracts with applying magnetic field at low temperatures. (e) Molar magnetization as a function of temperature ( $M$ - $T$  curve) measured under magnetic field  $H = 14$  T through both zero-field cooling (ZFC) and field cooling (FC) processes. (f) Molar magnetization as a function of magnetic field ( $M$ - $H$  curve) measured at 2 K and 80 K, respectively.

antiferromagnetic large-volume phase to ferromagnetic small-volume phase. The magnetization data [Figs. 4(e) and 4(f)], which shows that F moment reaches saturation below 14 T at 80 K, is in broad consistency with the magnetic-field NPD experiments. The saturation moment of  $1.35 \mu_B$  from the magnetization also agrees well with the zero-field NPD result [Fig. 1(d)].

Both hydrostatic-pressure and magnetic-field NPD experiments reveal that the antiferromagnetic large-volume phase and ferromagnetic small-volume phase may be the two separate energy minima in the  $x = 0.24$  sample. Therefore, the transition is presumably of discontinuous character, despite that it looks like a continuous phase transition [see Figs. 1(b) and 5(a)]. In the case of the discontinuous transition,

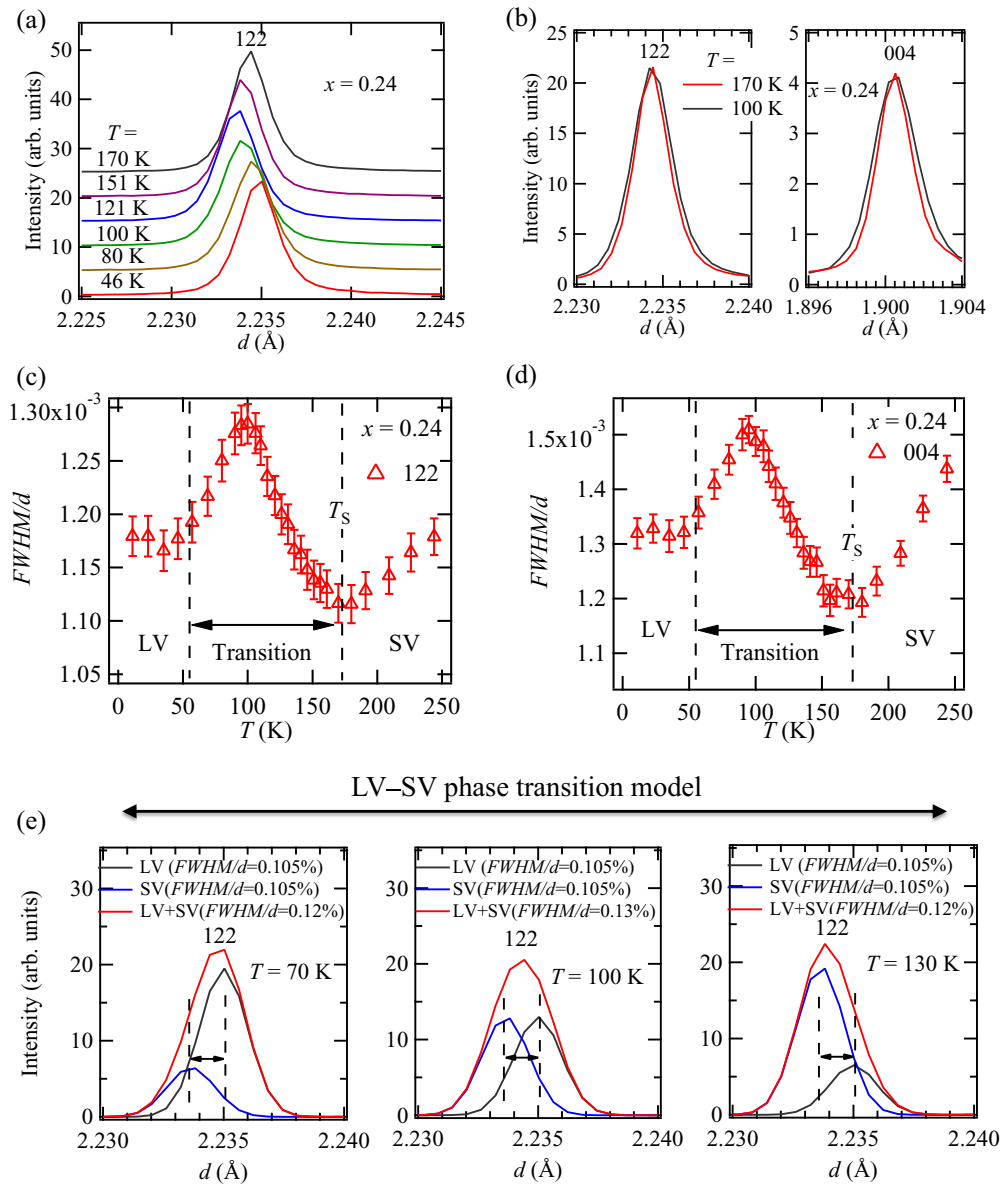


FIG. 5. High-resolution NPD on PrBaCo<sub>2</sub>O<sub>5.5+x</sub> ( $x = 0.24$ ). All the indices of reflections are given under the framework of nuclear unit cell ( $a_p \times 2a_p \times 2a_p$ ). (a) Diffraction profiles of the reflection 122 at different temperatures, showing the single peaks at all temperatures as well as the NTE. (b) Comparison of peak width at  $T = 100$  K and  $T = 170$  K for reflection 122 and reflection 004, respectively. The peaks are normalized to the same intensity and shifted to the same position for the better comparison. (c), (d) Full width at half maximum (FWHM) over  $d$ -spacing  $\frac{FWHM}{d}$  (relative peak width) of nuclear reflection 122 and reflection 004 as a function of temperature. The FWHMs are all derived from the Gaussian fitting to the NPD profiles. Anomalous peak broadening occurs with decrease in temperature, indicating the transition between FLISV phase and AFILV phase. (e) Simulation of the  $\frac{FWHM}{d}$ s of reflection 122 in panel (c) with the discontinuous large-volume (LV)–small-volume (SV) phase transition model. The  $\frac{FWHM}{d}$  of the single peak of LV (black line) or SV (blue line) is assumed to be 0.105% which is derived from the linear temperature dependence of  $\frac{FWHM}{d}$  in SV phase (above 170 K) in panel (c). The sum of the LV and SV peaks simulates the profile (red line) observed by NPD. By assigning proper peak position separation  $\Delta d_{122}$  and relative volume fractions, the  $\frac{FWHM}{d}$ s at 70 K, 100 K, and 130 K are well reproduced. The temperature evolution of volumes fractions follows the LV-SV phase transition.

coexistence of the two phases in the crossover region will bring about lattice inhomogeneities, inducing broadening or splitting of Bragg peak in the diffraction pattern. That is precisely what is measured in the high-resolution NPD experiment on the  $x = 0.24$  sample. As shown in Fig. 5(b), the nuclear reflections 122 and 004 are both broader at  $T = 100$  K than at  $T = 170$  K. The unusual peak broadening is ubiquitous in all Bragg peaks, indicating that the peak broadening comes from lattice inhomogeneities rather than lattice sym-

metry breaking. The temperature dependence of relative peak width [full width at half maximum (FWHM) over  $d$  spacing] [Figs. 5(c) and 5(d) show that the peaks starts to grow broader as the temperature is decreased to 170 K, reaches maximum width at 100 K, and returns to the normal breadth at about 50 K. Such unusual temperature dependence can be well described by the LV-SV phase transition model. As shown in Fig. 5(e), the experimental NPD profiles with different  $\frac{FWHM}{d}$ s at 70 K, 100 K, and 130 K are well reproduced by the sum

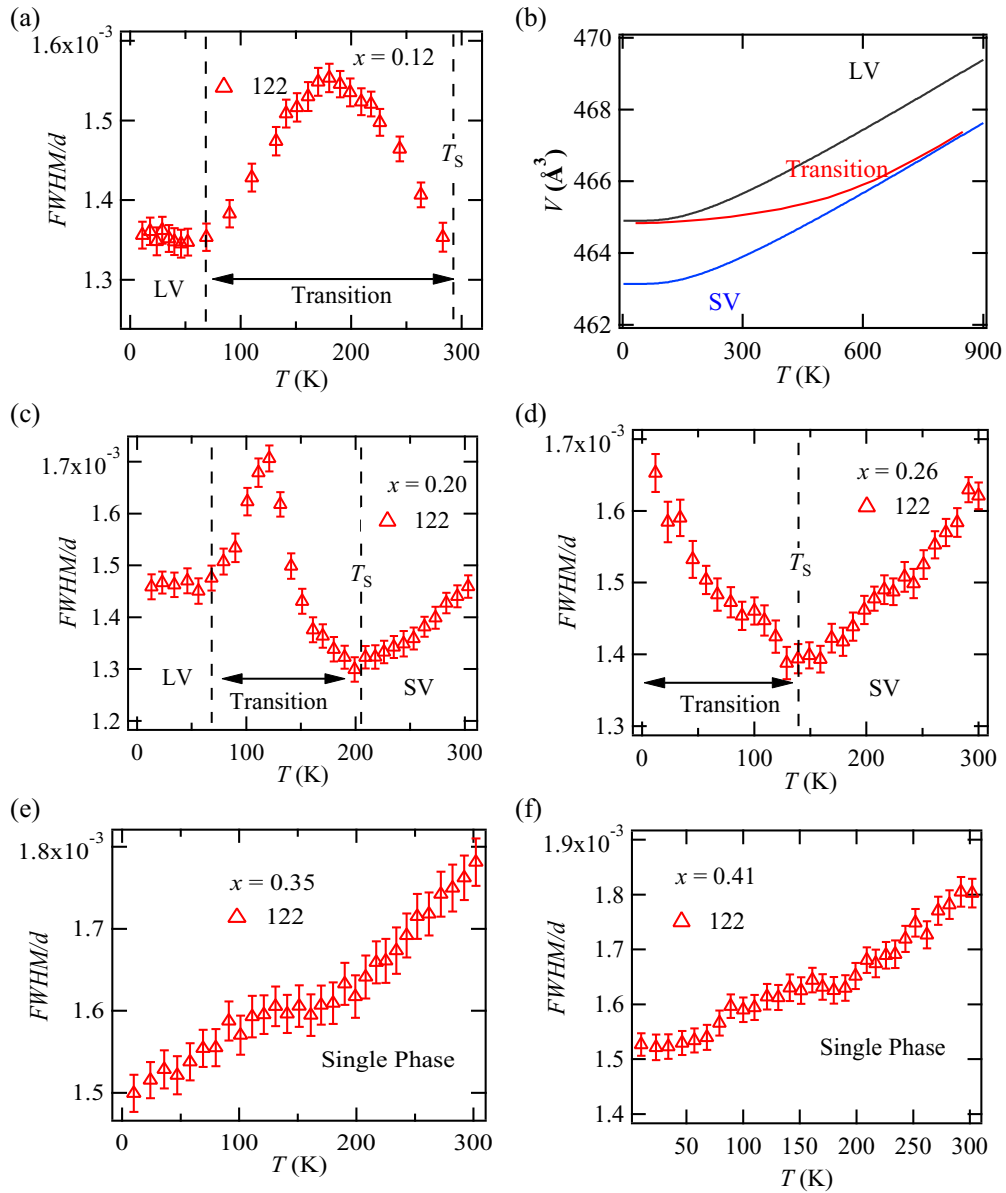


FIG. 6. High-resolution NPD on  $\text{PrBaCo}_2\text{O}_{5.5+x}$  ( $x = 0.12, 0.20, 0.26, 0.35,$  and  $0.41$ ) and transition model of  $x = 0.12$ . All the indices of reflections are given under the framework of nuclear unit cell ( $a_p \times 2a_p \times 2a_p$ ). (a), (c)–(f),  $\frac{\text{FWHM}}{d}$  (relative peak width) of nuclear reflection 122 as a function of temperature for hole-doping levels  $x = 0.12, 0.20, 0.26, 0.35,$  and  $0.41$ , respectively. The FWHMs are all derived from the Gaussian fitting to the NPD profiles. (b) The magnetoelectric transition model for NTE of  $x = 0.12$ , i.e., the transition from an AFILV phase to a FLISV phase.

of single LV and SV peak with different volume fractions, whose temperature evolution is consistent with LV-SV phase transition, i.e., the LV phase volume grows at the expense of SV phase volume upon cooling.

The peak broadening also occurs in other hole doping levels where anomalous thermal expansion occurs, e.g.,  $x = 0.12, 0.20, 0.25,$  and  $0.26$  as shown in Fig. 6. The temperature window could be as broad as from 70 K to 300 K at  $x = 0.12$ , giving nearly zero thermal expansion at low temperatures [Fig. 6(b)]. On the contrary, the FWHMs of those samples that show normal PTE, e.g.,  $x = 0.35$  and  $x = 0.41$  [Figs. 6(e) and 6(f)], have the monotonic temperature dependence. These results further corroborate that the unusual peak broadening

upon cooling corresponds to the coexistence of the LV and SV phases in the critical region.

Double-phase model of LV and SV was implemented in Rietveld refinement on the data where coexistence of the LV and SV phases are expected to occur, e.g., at  $T = 60$  K,  $H = 14$  T (Fig. 5) and at  $T = 100$  K,  $H = 0$  T (Fig. 6), and the results are compared with those of the single phase model as shown in Table I. The atomic positions and occupancy factors are constrained to be identical for LV and SV phases of the double-phase model so as to maintain a similar amount of variable parameters with the single-phase model. Although the single-phase model describes the data to a reasonable content in terms of the agreement factors  $R_{wp}$  (since neither peak

TABLE I. Structural details and agreement factors found from Rietveld refinement on the high-resolution NPD data of  $x = 0.24$  at different temperatures and magnetic fields. Both data used here exhibit anomalous peak broadening, which is attributed to the coexistence of LV and SV phases as shown in Fig. 5(e). For comparison, the results of single-phase model and double-phase model on the same data are listed, respectively. In the case of the double-phase model, atomic positions and occupancy factors are constrained to be identical for LV and SV phases. All the refinements have been done using the space group  $Pmmm$  and the unit cell of  $(a_p \times 2a_p \times 2a_p)$ . Wyckoff positions of different ions are  $2o$  (0.5,  $y$ , 0) for Ba;  $2p$  (0.5,  $y$ , 0.5) for Pr;  $2r$  (0, 0.5,  $z$ ) for Co1;  $2q$  (0, 0,  $z$ ) for Co2;  $1a$  (0, 0, 0) for O1;  $1e$  (0, 0.5, 0) for O2;  $1g$  (0, 0.5, 0.5) for O3;  $1c$  (0, 0, 0.5) for O4;  $2s$  (0.5, 0,  $z$ ) for O5;  $2t$  (0.5, 0.5,  $z$ ) for O6;  $4u$  (0,  $y$ ,  $z$ ) for O7. O3 and O4 are partially occupied and their occupancy factors are listed.

		$T = 60 \text{ K}, H = 14 \text{ T}$			$T = 100 \text{ K}, H = 0 \text{ T}$		
		Single phase	Double phases		Single phase	Double phases	
			LV	SV		LV	SV
$a$ (Å)		3.90468(2)	3.90505(3)	3.90107(5)	3.90383(1)	3.90554(2)	3.90318(3)
$b$ (Å)		7.81479(3)	7.81502(4)	7.81236(8)	7.81363(1)	7.81499(3)	7.81027(4)
$c$ (Å)		7.60407(3)	7.60486(4)	7.59871(8)	7.60050(1)	7.60294(3)	7.59834(4)
Ba	$y$	0.250(1)	0.249(2)	0.249(2)	0.252(1)	0.248(2)	0.248(2)
Pr	$y$	0.254(1)	0.250(2)	0.250(2)	0.253(1)	0.252(2)	0.252(2)
Co1	$z$	0.250(2)	0.248(3)	0.248(3)	0.251(2)	0.252(3)	0.252(3)
Co2	$z$	0.251(2)	0.251(3)	0.251(3)	0.252(2)	0.249(3)	0.249(3)
O3	occup.	0.82(2)	0.80(2)	0.80(2)	0.84(2)	0.85(2)	0.85(2)
O4	occup.	0.65(2)	0.67(2)	0.67(2)	0.64(2)	0.62(2)	0.62(2)
O5	$z$	0.290(2)	0.289(3)	0.289(3)	0.291(2)	0.288(3)	0.288(3)
O6	$z$	0.267(2)	0.267(3)	0.267(3)	0.268(2)	0.266(2)	0.266(2)
O7	$y$	0.248(2)	0.248(3)	0.248(3)	0.249(2)	0.250(2)	0.250(2)
	$z$	0.280(2)	0.278(3)	0.278(3)	0.280(2)	0.280(2)	0.280(2)
Mass ratio		100%	83.4(4)%	16.6(4)%	100%	48.8(1)%	51.2(1)%
$R_{wp}$		5.31%		4.19%	8.17%		5.75%

splitting nor peak-shape asymmetry occurs in the diffraction pattern), the double-phase model indeed gives better fitting to both data.

Further evidence for the two separated energy minima comes from the high-resolution diffraction experiment on the  $x = 0.25$  sample, where macroscopic phase separation was directly probed. As shown in Fig. 7, the nuclear reflection 122 starts to grow broader upon cooling down to 150 K and completely splits from about 50 K until base temperature, in conjunction with coexistence of the AF reflection  $\frac{1}{2}11$  and the F reflection 022 at base temperature. The peak splitting is also observed in many other Bragg peaks, ruling out the possibility of symmetry breaking of nuclear crystal structure. The whole pattern can be well fitted to the combination of the two-phase models [Fig. 7(d)], and the resultant volumes and mass ratios as a function of temperature are shown in Fig. 7(b).

### B. Magnetoresistance

In addition to the magnetoelastic coupling observed in the diffraction experiment, we also discovered a magnetoelectric coupling from the magnetoresistance measurement. As shown in Fig. 8, the low-temperature resistivity decreases upon applying magnetic field of 9 T for  $x = 0.24$  and 0.26, whereas the magnetic field barely influences the resistivity at other doping levels away from the antiferromagnetic-ferromagnetic boundary in the phase diagram. Such hole-doping dependence is more clearly demonstrated by the MR at low temperatures [Fig. 8(g)], which reaches maximum near the antiferromagnetic-ferromagnetic boundary. Therefore, the MR results indicate that the F phase is less insulating than

the AF phase. Taking into account the fact that the doping dependence of MVE also shows a peak centered near the antiferromagnetic-ferromagnetic phase boundary [Fig. 1(c)], the coincidence of MVE and magnetoresistance indicates a strong interplay among the properties of lattice, magnetism, and electronic transport, which induces the competing AFILV and FLISV ground states.

### C. $\mu$ SR

Since the crossover between the two energy minima is easily activated with a small amount of external energy (pressure, magnetic field, etc.), strong phase fluctuations are anticipated near the boundary at  $x \approx 0.24$ , for which we obtained direct evidence from muon-spin-relaxation ( $\mu$ SR) measurement. As shown in Figs. 9(a) and 9(b), dynamic fluctuations of Co spins at  $x = 0.24$  and 0.25 at base temperatures  $T = 4 \text{ K}$  and 6 K are identified from the decay of spectra under longitudinal field (LF) up to  $H = 0.4 \text{ T}$ . On the contrary, as shown in Figs. 9(c) and 9(d), the lack of time dependence in the spectra of the  $x = 0.35$  and  $x = 0.41$  samples even under the weak LF  $H = 0.01 \text{ T}$  suggests that all the Co spins are static at base temperatures. The difference unambiguously illustrates that the spin fluctuations, arising from the AFILV-FLISV phase fluctuations, become much stronger in the vicinity of the phase boundary than being away from it.

As shown in Fig. 9, the reduction in initial asymmetry  $A_s$  (at  $t = 0$ ) at zero field upon decreasing from high temperatures to base temperatures and the increase in  $A_s$  with applying LFs at base temperatures both indicate that all the samples contain a static phase with internal field at low

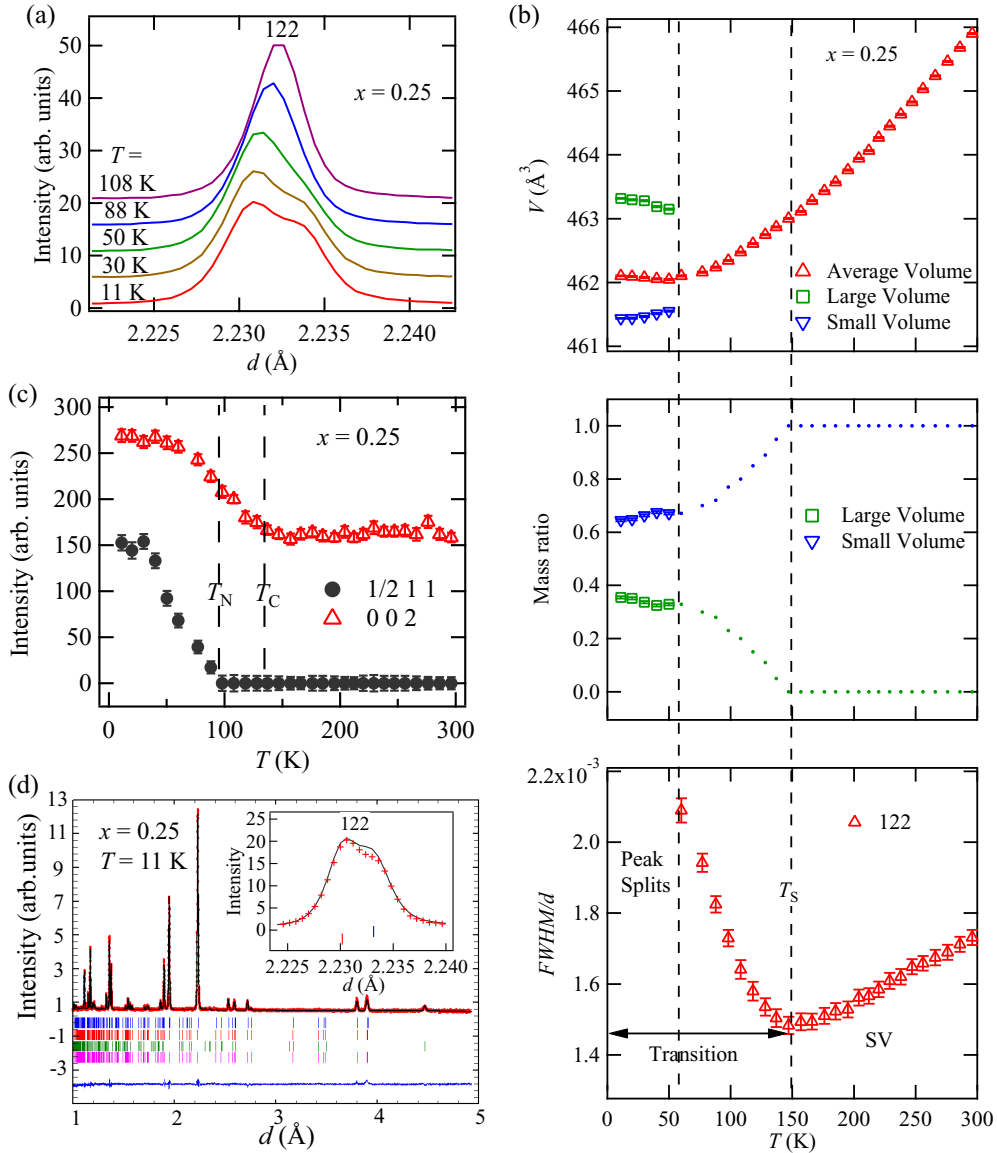


FIG. 7. High-resolution NPD on  $\text{PrBaCo}_2\text{O}_{5.5+x}$  ( $x = 0.25$ ). All the reflection indices are given under the unit-cell framework ( $a_p \times 2a_p \times 2a_p$ ). (a) Diffraction profiles of the reflection 122 at different temperatures. Peak splitting occurs in reflection 122 (and others) at low temperatures, indicating macroscopic phase separation of the AFILV phase and the FLISV phase. (b) Sub unit cell ( $2a_p \times 2a_p \times 2a_p$ ) volume, mass ratio, and  $\frac{\text{FWHM}}{d}$  of nuclear reflection 122 as a function of temperature. The  $\frac{\text{FWHM}}{d}$  of the bottom panel was calculated from the single reflection 122 until it splits into two at about  $T = 50$  K [panel (a)], below which the pattern was described by Rietveld refinement with the model of double phases [panel (d)], the FLISV phase and the AFILV phase. The resultant volume ( $2a_p \times 2a_p \times 2a_p$ ) and mass ratio as a function of temperature are shown in top and middle panels. The averaged volume is calculated by  $V_{\text{average}} = R_{\text{AFILV}} \times V_{\text{AFILV}} + R_{\text{FLISV}} \times V_{\text{FLISV}}$ , where  $R$  is the mass ratio. (c) Integrated intensities of antiferromagnetic reflection  $\frac{1}{2}11$  and ferromagnetic reflection 002 as a function of temperature, showing the coexistence of antiferromagnetic and ferromagnetic phases. (d) Rietveld refinement on the data at  $T = 11$  K using the model of double phases (FLISV and AFILV). The ferromagnetic and antiferromagnetic structure models are shown in Fig. 1(e). Experimental data points are shown by red dots, and the black line through them is a fit by Rietveld analysis. Red (magenta) bars denote the indices from nuclear (magnetic) structures of FLISV while blue (green) bars represent the indices from nuclear (magnetic) structures of AFILV phase. Blue line shows the difference between experiment and calculation. The residual value  $R_{wp}$  is 5.95% and  $R_M$  is 23.0%.

temperatures, corresponding to the long-range Co-spin orders that were detected by NPD [21]. The magnetic volume fractions for both dynamic and static phases can be derived by taking advantage of the spectra under the  $H = 0.01$  T, which decouples the decay from nuclear moments with least disturbance to the contributions from Co moments. Since the background is negligible according to the high-temperature spectra [Figs. 9(e)–9(g)], the spectra under  $H = 0.01$  T can

be fitted to the following equation:

$$A_s G_z(H, t) = A_1 \exp[-\Lambda t] + A_2 \left[ \frac{1}{3} + \frac{2}{3} \cos(\gamma_\mu B t) \right], \quad (1)$$

where  $A_1$  and  $A_2$  parametrize the contributions from dynamic and static phases, respectively. The oscillation could not be observed due to the limitation of the time resolution of pulsed muon source, and the term  $\cos(\gamma_\mu B t)$  is averaged to 0 here. The temperature dependence of magnetic volume fractions

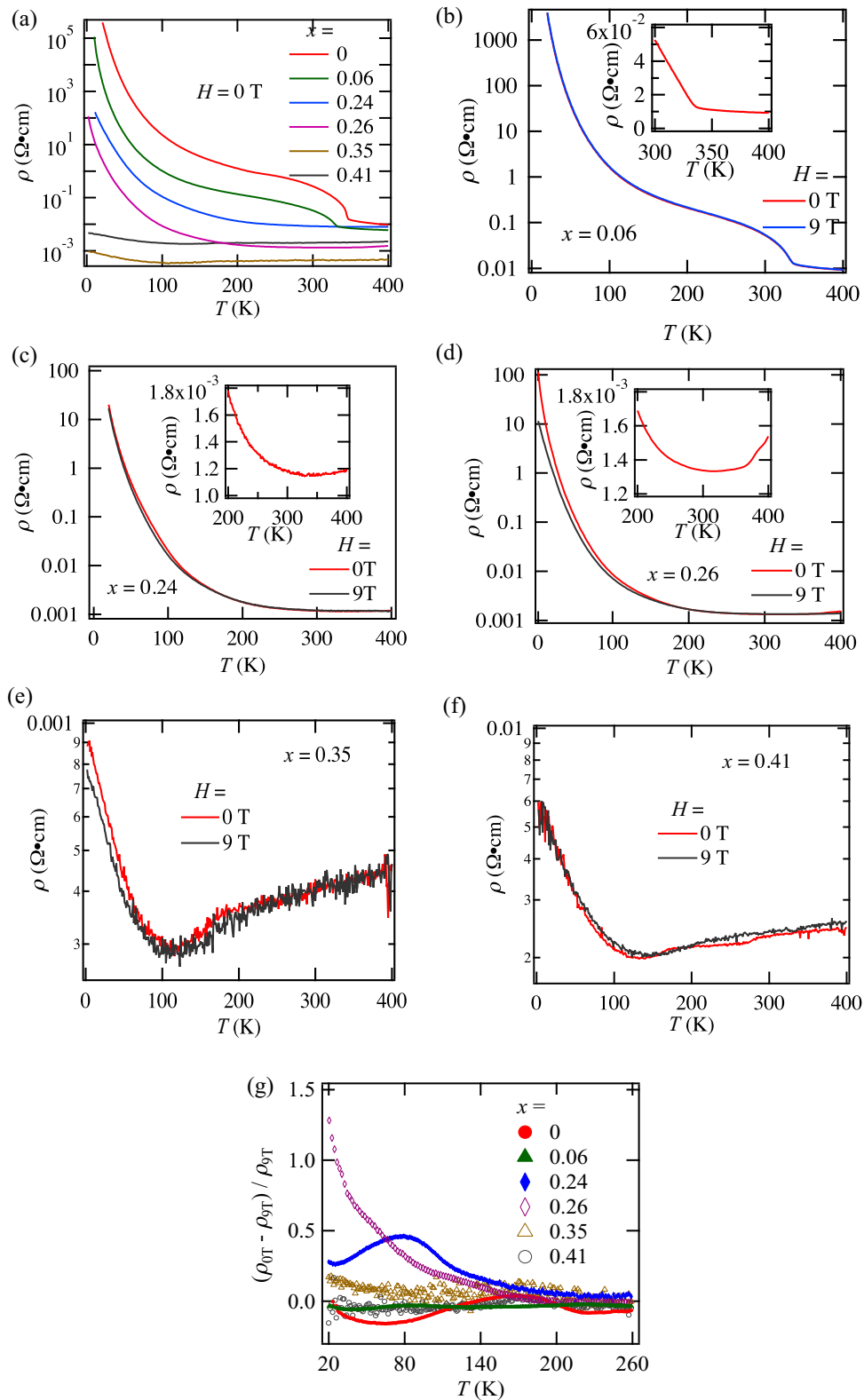


FIG. 8. Resistivity measurement of PrBaCo<sub>2</sub>O<sub>5.5+x</sub>. (a) Resistivity as a function of temperature measured under zero magnetic field at various hole doping levels, which shows a sharp decrease in resistivity with increasing hole doping. The relatively lower value in  $\rho$  for  $x = 0.26$  and  $0.35$  than other hole doping  $x$  is possibly due to the lower boundary resistance of polycrystal grains compared with that in samples with other hole-doping fractions. (b)–(f) Resistivity as a function of temperature measured under zero magnetic field and  $H = 9$  T for  $x = 0.06$ ,  $x = 0.24$ ,  $x = 0.26$ ,  $x = 0.35$ , and  $x = 0.41$ , respectively. The insets in (b)–(d) show the resistivity under zero field in a focused temperature window. (g) Magnetoresistance calculated from the relative resistivity difference between  $H = 0$  T and  $9$  T as a function of temperature at various hole-doping level  $x$ , which shows that the strongest magnetoresistance occurs near the doping level of the AF-F phase boundary.

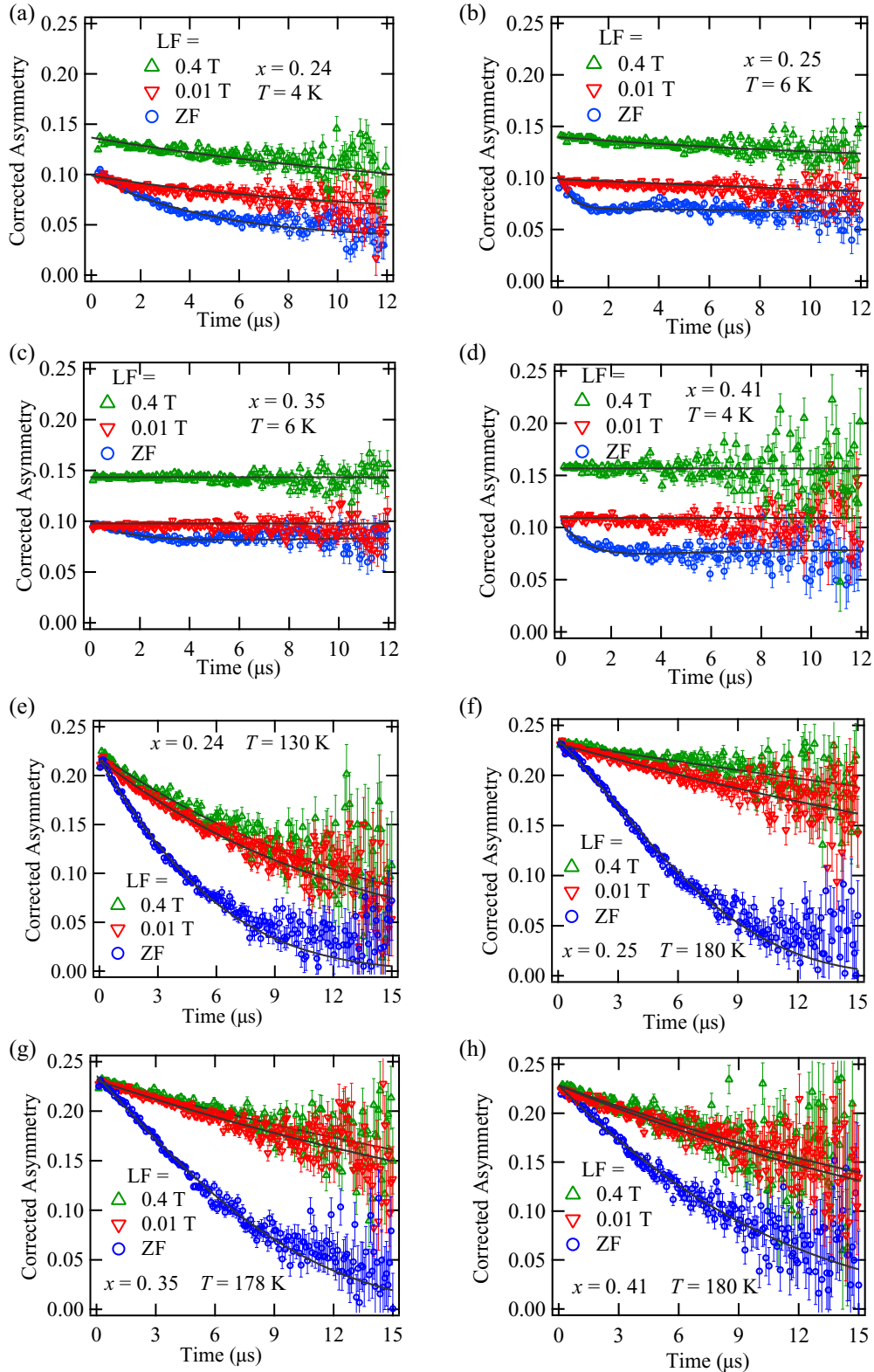


FIG. 9. Muon spin relaxation ( $\mu$ SR) measurements of  $\text{PrBaCo}_2\text{O}_{5.5+x}$  ( $x = 0.24, 0.25, 0.35$ , and  $0.41$ ). (a)–(d),  $\mu$ SR spectra of  $x = 0.24$  at  $T = 4$  K (a),  $x = 0.25$  at  $6$  K (b),  $x = 0.35$  at  $6$  K (c), and  $x = 0.41$  at  $4$  K (d) under various longitudinal fields (LFs). The spectrum of zero field at long  $t$  is significantly lifted up with application of a weak LF  $0.01$  T, which arises from the decoupling of muon from the nuclear moments or spin glass component. The fitting equation for describing the zero-field (ZF) spectrum is  $A_s G_z(H, t) = G_{\text{GKT}}(t) \{A_1 \exp[-\Delta t] + A_2 [\frac{1}{3} + \frac{2}{3} \cos(\gamma_\mu B t)]\}$  for  $x = 0.24, 0.25$ , and  $0.35$ , and  $A_s G_z(H, t) = G_{\text{LKT}}(t) \{A_1 \exp[-\Delta t] + A_2 [\frac{1}{3} + \frac{2}{3} \cos(\gamma_\mu B t)]\}$  for  $x = 0.41$ , where  $G_{\text{GKT}}(t)$  is the Gaussian Kubo-Toyabe relaxation function (nuclear moments distribution),  $G_{\text{LKT}}(t)$  the Lorentzian Kubo-Toyabe relaxation function (spin glass component), and the other terms are described in the main text for Eq. (1). In all samples, the spectra under LFs are fitted to Eq. (1) because the nuclear moment component [ $G_{\text{GKT}}(t)$ ] and spin glass component [ $G_{\text{LKT}}(t)$ ] are fully decoupled by LFs. All the fittings are shown

calculated from  $A_1$  and  $A_2$ , and the damping rate  $\Lambda$  (Fig. 10) reveals that the Co spins at  $x = 0.41$  become completely static as the temperature is decreased to 80 K whereas the spin fluctuations at  $x = 0.24$  survive until the base temperature, which again corroborates the strong phase fluctuation near the phase boundary.

#### D. DFT calculations

We also found theoretical support for the AFILV-FLISV transition scenario. As shown in Fig. 11(c), the density-functional-theory (DFT) calculations on  $x = 0.25$  demonstrate that an electronic gap is open at the Fermi level of the antiferromagnetic state while the Fermi level in the ferromagnetic state becomes gapless, resulting in the magnetoresistance property. Although our experimental observation shows the insulating behavior in FLISV phase, the metallic behavior observed at high temperatures (Fig. 8) also suggests that the gap of insulating ground state could be very small. Therefore, the DFT calculation is in broad agreement with the experiment given that the calculated density of states at the Fermi level of the ferromagnetic state is quite low. The volume dependence of the total energy in Fig. 11(d) shows separate minima of antiferromagnetic and ferromagnetic state, respectively, where the unit cell volume of the energy minimum of the antiferromagnetic state is  $463.74 \text{ \AA}^3$  and that of the ferromagnetic state is  $460.94 \text{ \AA}^3$ . Therefore, the AFILV and FLISV ground states are reproduced by the DFT calculations.

#### IV. DISCUSSION

With compelling evidence from multiple techniques, we unveil the microscopic origin for the volume-magnetism correlation in  $\text{PrBaCo}_2\text{O}_{5.5+x}$ . Specifically, giant competition between the AFILV phase and the FLISV phase occurs in the vicinity of the phase boundary, so that dramatic magnetoelastic and magnetoelectric responses can be driven by moderate external stimuli such as temperature, hole doping, hydrostatic pressure, and magnetic field, etc. As a result, the anomalous NTE [Fig. 1(a)] originate from the temperature-induced AFILV-FLISV transition. The strong competition between AFILV and FLISV ground states manifests itself in the NPD, magnetoresistance, and  $\mu\text{SR}$  experiments as well as the DFT calculations. Although the FLISV ground state is not metallic, its electron conductivity does differ from that of the AFILV phase. One evidence is the strongest magnetoresistance at 2 K near the phase boundary (at  $x = 0.26$ ); the other is the strongest magnetoresistance of  $x = 0.24$  occurs at about 80 K, which is consistent with our high-field NPD result that AF phase is converted to F phase by 14 T field to the largest content at 80 K [see Fig. 4(c)]. From the unit cell volume change under high pressures of 0.8 GPa as shown in Fig. 2(f), the energy change per subcell ( $2a_p \times 2a_p \times 2a_p$ ) is  $\sim 18.8$  meV. From the magnetic moment change under high

field of 14 T as shown in Fig. 4(a), the energy change per subcell is less than 3.2 meV. On the other hand, the DFT calculations indicates that the energy difference between the two phases is about 900 meV per subcell, much larger than the experimental results. Therefore, the DFT calculations only qualitatively explain the AFILV and FLISV ground states.

The coexistence of two phases in the anomalous thermal expansion regions of the samples ( $x = 0.12, 0.20, 0.24, 0.25$ , and  $0.26$ ) are evidenced from ubiquitous broadening of Bragg peaks upon cooling in the high-resolution NPD experiment. The peak broadening might develop into peak splitting when the relatively peak width  $\frac{\text{FWHM}}{d}$  is over 0.20% within the present instrument resolution, which was observed in the  $x = 0.25$  sample. Accordingly, the AFILV-FLISV transition is intrinsic of discontinuous character, despite that it looks like a continuous phase transition from the volumetric and magnetic order parameters [21]. Weak discontinuous phase transitions were often characterized as continuous under the normal experimental precision, and the conclusion can be overturned by higher-precision measurements [39].  $\text{PrBaCo}_2\text{O}_{5.5+x}$  constitutes such a case as well and the merit of high resolution allows us to finally determine the correct transition type. Based on our simulation of peak broadening of  $x = 0.24$  in Fig. 5(e), the peak shift  $\frac{\Delta d_{122}}{d_{122}}$  between AFILV and FLISV phases is about 0.06%, corresponding to the volume difference of unit cell ( $2a_p \times 2a_p \times 2a_p$ ) of  $\sim 1 \text{ \AA}^3$  (derived from the relation of  $\frac{\Delta a}{a} = \frac{\Delta b}{b} = \frac{\Delta c}{c} = \frac{\Delta d_{122}}{d_{122}}$ ). On the other hand, the volume difference derived from Debye-Grüneisen model in Fig. 1(e) is  $\sim 2 \text{ \AA}^3$ . We think the difference is related to a large uncertainty in Debye temperature  $\theta_D$ , which is reported to range from 227 K to 660 K [40,41]. The volume difference in Fig. 1(e) can be reduced to  $\sim 1 \text{ \AA}^3$  by modifying the  $\theta_D$ .

In the AFILV phase, superexchange antiferromagnetic interaction dominates magnetic correlation between the Co ions, leading a tendency towards the insulating behavior, and with additional help from longer atomic distance, the insulating ground state is stabilized. As for the FLISV phase, the Co ions are mainly correlated by double-exchange ferromagnetic interaction which prefers the itinerant charge transport, and the shorter atomic distance further helps to stabilize the less insulating ground state. To be noted, the volume difference between AFILV and FLISV phases is not related to change of spin state of  $\text{Co}^{3+}$  ions, i.e., the size of magnetic moment, since experimentally we did not observe nominal change in the magnetic moment size at 10 K across the boundary of the two phases [Fig. 1(d)]. Compared with most MVE materials like Invar alloys [2,5], trivalent manganese fluoridite [42], manganites [43], antiperovskite manganese nitrides [44–46], intermetallics [47–49], etc., where the MVE originates from the coupling between spin and lattice degrees of freedom,  $\text{PrBaCo}_2\text{O}_{5.5+x}$  exhibits an unusual volume-magnetism correlation where the spin, charge, and lattice degrees of freedom are all intimately connected so that MVE and ME occur

← as the solid lines. (e)–(h)  $\mu\text{SR}$  spectra of  $x = 0.24$  at  $T = 130$  K (e),  $x = 0.25$  at 180 K (f),  $x = 0.35$  at 178 K (g), and  $x = 0.41$  at 180 K (h) under various longitudinal fields (LFs). The zero-field (ZF) spectra indicate that the background is negligible. Since all spectra were collected above magnetic ordering temperatures, only the dynamic spin fluctuation and nuclear spin distribution were taken into account and all the spectra are fitted to the equation  $A_z G_z(H, t) = A_1 \exp[-\Lambda t] G_{\text{GKT}}(t)$ , where  $G_{\text{GKT}}(t)$  amounts to 0 under LFs since  $G_{\text{GKT}}(t)$  is fully decoupled by LFs. The solid lines show the fittings.

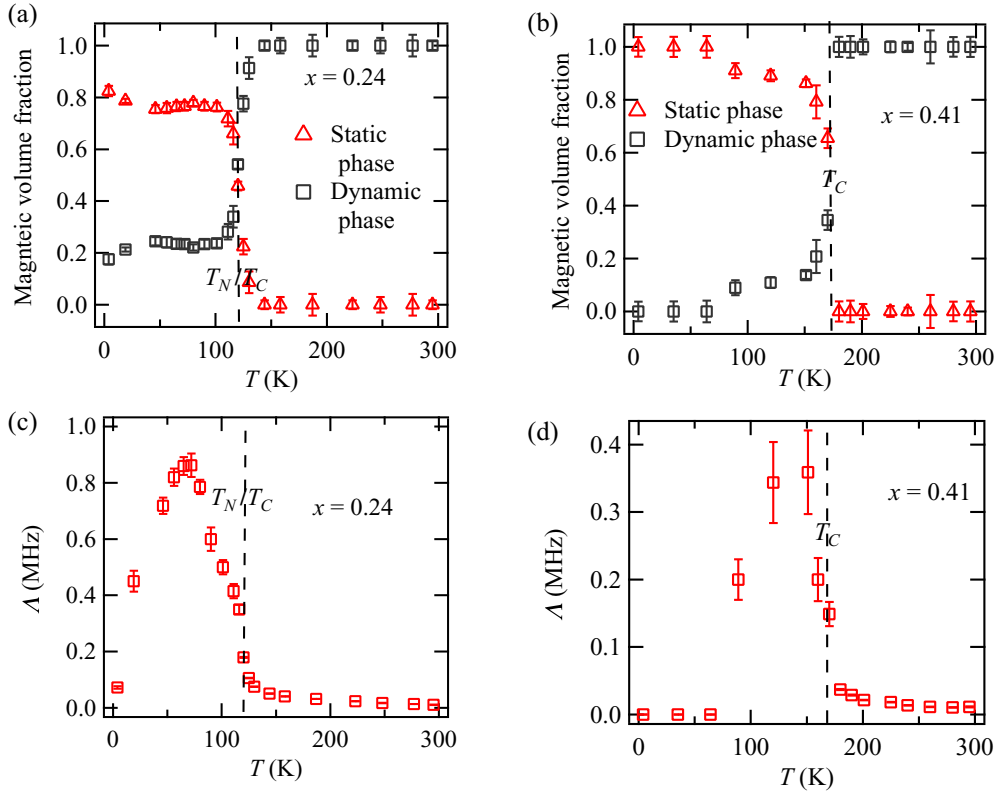


FIG. 10. Muon spin relaxation ( $\mu$ SR) measurements of  $\text{PrBaCo}_2\text{O}_{5.5+x}$  ( $x = 0.24$  and  $0.41$ ). (a),(b) Magnetic volume fractions as a function of temperature for  $x = 0.24$  (a) and  $x = 0.41$  (b), derived from fraction (dynamic phase)  $= \frac{A_1}{A_1+A_2}$  and fraction (static phase)  $= \frac{A_2}{A_1+A_2}$ , where  $A_1$  and  $A_2$  are obtained from the fittings of the spectra under LF of 0.01 T to Eq. (1). (c),(d) Temperature dependence of muon spin-lattice-relaxation rate  $\Lambda$  for  $x = 0.24$  (c) and  $x = 0.41$  (d), derived from fittings of the spectra under LF of 0.01 T to Eq. (1). The  $\Lambda$  for  $x = 0.41$  reduces to 0 upon cooling down to about 80 K, which is commonly observed in those materials showing magnetic ordering. However, the  $\Lambda$  for  $x = 0.24$  shows unusual behavior, i.e., it stays nonzero even down to the base temperature. The results imply that the strong phase fluctuations occur at  $x = 0.24$  so that the related dynamic spin fluctuations survive until the base temperature.

simultaneously. Our study unveils a different mechanism for the MVE and opens an alternative path to the design of MVE materials.

Among the ME materials, such as CMR or multiferroic compounds,  $\text{PrBaCo}_2\text{O}_{5.5+x}$  is a rare example that the symmetry of the crystal structure survives in the AFILV-FLISV transition. In manganites with CMR effect, charge and/or orbital ordering stabilize the antiferromagnetic insulating phase. Charge ordering brings about the loss of translation symmetry, and orbital ordering couples with Jahn-Teller distortion so that the antiferromagnetic insulating phase resides in a low-symmetry crystal structure. Applying magnetic field can melt the orders and transform it into a high-symmetry ferromagnetic metallic phase [19,20]. In multiferroics, the magnetic ordering causes through inverse Dzyaloshinskii-Moriya interaction the structural distortion, which breaks the inversion symmetry and induces the electronic polarization [24,25]. The ME in  $\text{PrBaCo}_2\text{O}_{5.5+x}$  does not require either charge/orbital ordering or inversion symmetry breaking because the charge transport property can be significantly influenced by the unit cell volume. Therefore, our study here demonstrates a different way of generating ME.

The easy AFILV-FLISV phase conversion gives the cobaltite broad tunability of average volume via multiple external stimuli. The broad tunability can be utilized to realizing

zero thermal expansion in a wide temperature window, which is of great importance for industrial use [50,51]. For example, reducing the doping level  $x$  from 0.24 to 0.12 opens a wider temperature window of transition [50–170 K at  $x = 0.24$ , see Fig. 5(d); 70–300 K at  $x = 0.12$ , see Fig. 6(a)] and transforms the NTE into the nearly zero thermal expansion. What could be more interesting is that moderate magnetic field, hydrostatic pressure, or combination of both will simultaneously produce multiple responses from the lattice, magnetism, and charge transport properties. The multiple responses are promising for technical applications like magnetic/pressure sensors, actuators, transducers, and so on.

#### ACKNOWLEDGMENTS

We acknowledge the merit award of beam time for neutron and muon experiments at Japan Proton Accelerator Research Complex (J-PARC). The neutron scattering experiment was approved by the Neutron Science Proposal Review Committee of J-PARC/MLF (Proposals No. 2014S05 for SuperHRPD, No. 2017B0062 for PLANET, No. 2017A0014 and 2017B0045 for S-line) and supported by the Inter-University Research Program on Neutron Scattering launched by Institute of Materials Structure Science, High Energy Accelerator Research Organization. We thank Prof. Sumio Ishihara, Dr.

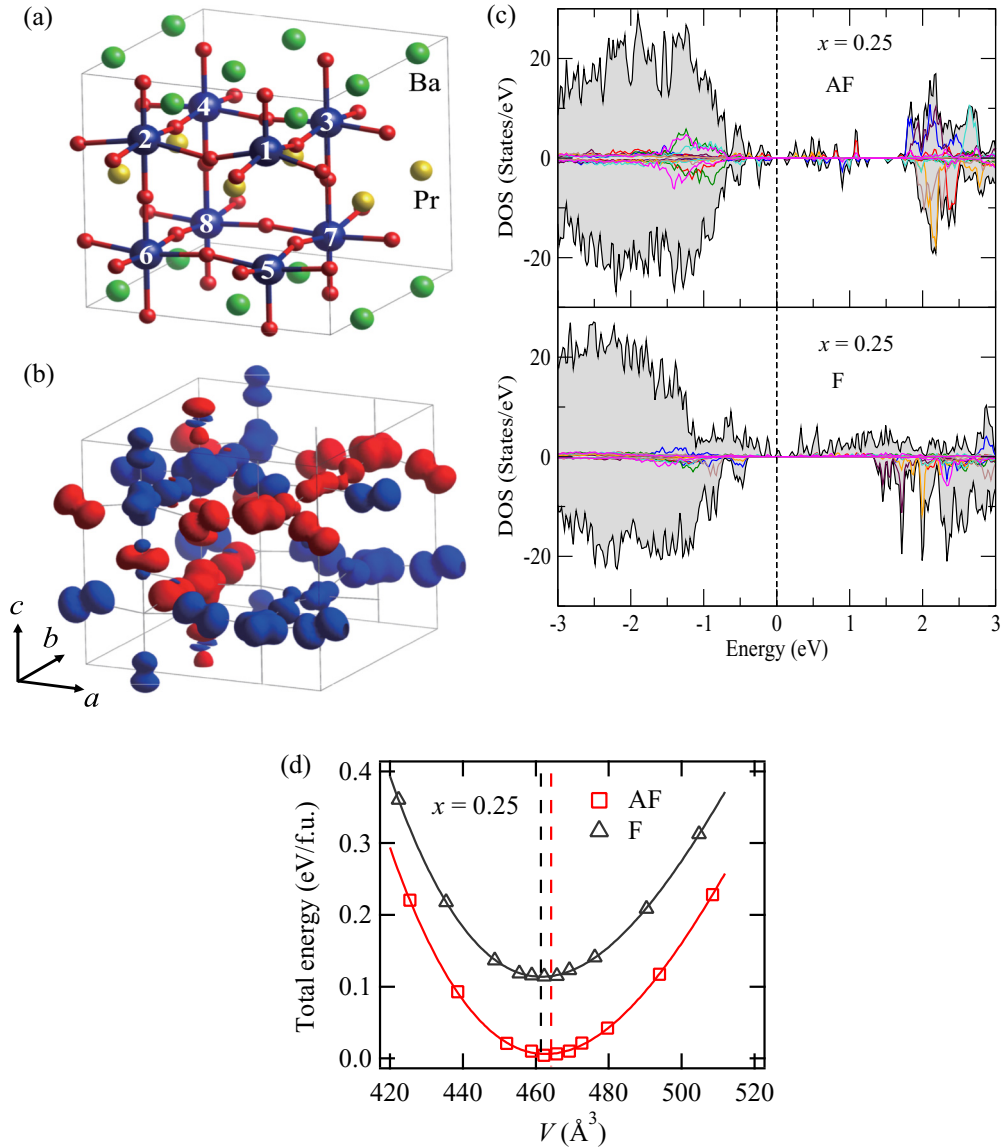


FIG. 11. DFT calculations of  $\text{PrBaCo}_2\text{O}_{5.5+x}$  ( $x = 0.25$ ). (a) Sub unit cell ( $2a_p \times 2a_p \times 2a_p$ ) used in DFT calculations. Numbers indicate Co site index. An apical oxygen atom located between Co1 and Co5 is removed to mimic the oxygen vacancy. (b) Spin density (blue: up-spin and red: down-spin state) of Co-3d orbital states in an energy range of  $E_F - 0.5 \text{ eV} < E < E_F$  in the antiferromagnetic (AF) state. (c) Density of states for antiferromagnetic (AF, upper panel) and ferromagnetic (F, lower panel) states of  $x = 0.25$ , showing the antiferromagnetic state has an open gap while the ferromagnetic phase is gapless. The dashed line denotes Fermi level. The black shadowed lines show the total density of states and the colored lines indicate the contribution from each of the eight Co sites in the nuclear subcell ( $2a_p \times 2a_p \times 2a_p$ ). (d) Calculated total energies for the AF and F states as a function of cell volume, fitted to a polynomial function to derive the energy minima as shown by dashed lines.

Yukio Noda, Dr. Masatoshi Hiraishi and Dr. Soshi Takeshita, Dr. Yang Ren, Dr. Jiaxin Zheng, Dr. Mouyi Wen, and Zongxiang Hu for helpful discussions. We also appreciate Dr. Hiro-taka Okabe, Dr. Motoyuki Ishikado, Dr. Taketo Moyoshi, Dr. Masato Hagihara, Masahiro Shioya, Widya Rika, and Nur Ayu for their assistance with the experiments and data analysis.

#### APPENDIX: DETAILS OF CALCULATIONS OF UNIT CELL VOLUME USING THE DEBYE-GRUNEISEN MODEL

The calculated volumes of unit cell ( $2a_p \times 2a_p \times 2a_p$ ) in Figs. 1(b), 1(c), and 1(e) are based on the Debye-Gruneisen

model which characterizes the phonon contribution to anharmonic thermal expansion [52]. The formula is expressed in Eq. (A1):

$$V(T) = V_{0,0} \left[ 1 + \frac{E(T)}{Q - aE(T)} \right], \quad (\text{A1})$$

where  $V_{0,0}$  is the unit cell volume at ambient pressure and zero temperature,  $a = \frac{1}{2}(B'_{0,0} - 1)$ , and  $Q = (V_{0,0}B_{0,0}/\gamma)$ .  $B_{0,0}$  is the isothermal bulk modulus at ambient pressure and zero temperature and  $B'_{0,0}$  is its first derivative with respect to pressure.  $\gamma$  is the thermal Gruneisen parameter.  $E(T)$  is the internal energy contributed by phonons, which is expressed in

Eq. (A2):

$$E(T) = \frac{9nk_B T}{(\theta_D/T)^3} \int_0^{\theta_D/T} \frac{x^3}{e^x - 1} dx \quad (\text{A2})$$

where  $\theta_D$  is the Debye temperature,  $n$  is the number of atoms per unit cell, and  $k_B$  is the Boltzmann constant.

In the calculations for different samples or phases, we maintain consistent values for  $\theta_D$ ,  $Q$ , and  $a$ , with only  $V_{0,0}$  being variable, where  $\theta_D \approx 235$  K,  $Q \approx 2.3 \times 10^{-17} J$ , and  $a \approx 1.5$ . An uncertainty exists in Debye temperature  $\theta_D$ , which is reported to range from 227 K to 660 K [40,41]. The  $Q$  and  $a$  are close to those used in similar systems [53].

- 
- [1] C. E. Guillaume, C. R. Acad. Sci. **125**, 235 (1897).
- [2] E. F. Wasserman, *Ferromagnetic Materials. Chapter 3* (Elsevier Science Publisher B.V., Amsterdam, 1990).
- [3] Y. Nakamura, *IEEE Trans. Magn. Mag* **12**, 278 (1976).
- [4] R. J. Weiss, *Proc. Phys. Soc.* **82**, 281 (1963).
- [5] T. Moriya and K. Usami, *Solid State Commun.* **34**, 95 (1980).
- [6] K. Lagarec, D. Rancourt, S. Bose, B. Sanyal, and R. Dunlap, *J. Magn. Magn. Mater.* **236**, 107 (2001).
- [7] F. Liot and I. A. Abrikosov, *Phys. Rev. B* **79**, 014202 (2009).
- [8] A. V. Ruban, S. Khmelevskiy, P. Mohn, and B. Johansson, *Phys. Rev. B* **76**, 014420 (2007).
- [9] V. Crisan, P. Entel, H. Ebert, H. Akai, D. D. Johnson, and J. B. Staunton, *Phys. Rev. B* **66**, 014416 (2002).
- [10] J. Kaspar and D. R. Salahub, *Phys. Rev. Lett.* **47**, 54 (1981).
- [11] S. Khmelevskiy, I. Turek, and P. Mohn, *Phys. Rev. Lett.* **91**, 037201 (2003).
- [12] E. I. Kondorsky and V. L. Sedov, *J. Appl. Phys.* **31**, S331 (1960).
- [13] D. G. Rancourt and M.-Z. Dang, *Phys. Rev. B* **54**, 12225 (1996).
- [14] M. van Schilfgaarde, I. A. Abrikosov, and B. Johansson, *Nature (London)* **400**, 46 (1999).
- [15] H. Hasegawa, *Physica B+C* **119**, 15 (1983).
- [16] F. Liot and C. A. Hooley, [arXiv:0811.3673](https://arxiv.org/abs/0811.3673).
- [17] J. B. Staunton, D. D. Johnson, and B. L. Gyorffy, *J. Appl. Phys.* **61**, 3693 (1987).
- [18] P. A. Lee, N. Nagaosa, and X.-G. Wen, *Rev. Mod. Phys.* **78**, 17 (2006).
- [19] Y. Tokura, *Rep. Prog. Phys.* **69**, 797 (2006).
- [20] E. Dagotto, T. Hotta, and A. Moreo, *Phys. Rep.* **344**, 1 (2001).
- [21] P. Miao, X. Lin, A. Koda, S. Lee, Y. Ishikawa, S. Torii, M. Yonemura, T. Mochiku, H. Sagayama, S. Itoh, K. Ikeda, T. Otomo, Y. Wang, R. Kadono, and T. Kamiyama, *Adv. Mater.* **29**, 1605991 (2017).
- [22] P. Miao, X. Lin, S. Lee, Y. Ishikawa, S. Torii, M. Yonemura, T. Ueno, N. Inami, K. Ono, Y. Wang, and T. Kamiyama, *Phys. Rev. B* **95**, 125123 (2017).
- [23] C. Frontera, J. L. García-Muñoz, A. E. Carrillo, C. Ritter, D. Martín y Marero, and A. Caneiro, *Phys. Rev. B* **70**, 184428 (2004).
- [24] S.-W. Cheong and M. Mostovoy, *Nat. Mater.* **6**, 13 (2007).
- [25] D. Khomskii, *Physics* **2**, 20 (2009).
- [26] S. Torii, M. Yonemura, T. Yulius Surya Panca Putra, J. Zhang, P. Miao, T. Muroya, R. Tomiyasu, T. Morishima, S. Sato, H. Sagehashi, Y. Noda, and T. Kamiyama, *J. Phys. Soc. Jpn.* **80**, SB020 (2011).
- [27] T. Hattori, A. Sano-Furukawa, H. Arima, K. Komatsu, A. Yamada, Y. Inamura, T. Nakatani, Y. Seto, T. Nagai, W. Utsumi, T. Iitaka, H. Kagi, Y. Katayama, T. Inoue, T. Otomo, K. Suzuya, T. Kamiyama, M. Arai, and T. Yagi, *Nucl. Instrum. Methods Phys. Res., Sect. A* **780**, 55 (2015).
- [28] K. Komatsu, M. Moriyama, T. Koizumi, K. Nakayama, H. Kagi, J. Abe, and S. Harjo, *High Press. Res.* **33**, 208 (2013).
- [29] T. Strässle, S. Klotz, K. Kunc, V. Pomjakushin, and J. S. White, *Phys. Rev. B* **90**, 014101 (2014).
- [30] J. Rodríguez-Carvajal, *Physica B* **192**, 55 (1993).
- [31] A. Wills, *Physica B* **278**, 680 (2000).
- [32] R. Oishi, M. Yonemura, Y. Nishimaki, S. Torii, A. Hoshikawa, T. Ishigaki, T. Morishima, K. Mori, and T. Kamiyama, *Nucl. Instrum. Methods Sect. A* **600**, 94 (2009).
- [33] R. Oishi-Tomiyasu, M. Yonemura, T. Morishima, A. Hoshikawa, S. Torii, T. Ishigaki, and T. Kamiyama, *J. Appl. Crystallogr.* **45**, 299 (2012).
- [34] A. Suter and B. Wojek, *Phys. Procedia* **30**, 69 (2012), 12th International Conference on Muon Spin Rotation, Relaxation and Resonance (SR2011).
- [35] G. Kresse and J. Furthmüller, *Phys. Rev. B* **54**, 11169 (1996).
- [36] J. Heyd, G. E. Scuseria, and M. Ernzerhof, *J. Chem. Phys.* **118**, 8207 (2003).
- [37] A. Stroppa and S. Picozzi, *Phys. Chem. Chem. Phys.* **12**, 5405 (2010).
- [38] K. Yamauchi and S. Picozzi, *Phys. Rev. Lett.* **105**, 107202 (2010).
- [39] S. Yang, X. Ren, and X. Song, *Phys. Rev. B* **78**, 174427 (2008).
- [40] J. Wiecekowsk, M. U. Gutowska, A. Szewczyk, S. Lewinska, K. Conder, E. Pomjakushina, V. P. Gnezdilov, and S. L. Gnatchenko, *Phys. Rev. B* **86**, 054404 (2012).
- [41] K. Knížek, J. c. v. Hejtmánek, Z. c. v. Jiráček, P. Tomeš, P. Henry, and G. André, *Phys. Rev. B* **79**, 134103 (2009).
- [42] B. A. Hunter, B. J. Kennedy, and T. Vogt, *Phys. Rev. B* **69**, 020410(R) (2004).
- [43] J. García-Muñoz, M. Suaaidi, and C. Ritter, *Phys. B: Condens. Matter* **234-236**, 854 (1997), proceedings of the First European Conference on Neutron Scattering.
- [44] K. Takenaka and H. Takagi, *Appl. Phys. Lett.* **87**, 261902 (2005).
- [45] X. G. Guo, J. C. Lin, P. Tong, M. Wang, Y. Wu, C. Yang, B. Song, S. Lin, W. H. Song, and Y. P. Sun, *Appl. Phys. Lett.* **107**, 202406 (2015).
- [46] S. Deng, Y. Sun, H. Wu, Q. Huang, J. Yan, K. Shi, M. I. Malik, H. Lu, L. Wang, R. Huang, L. Li, and C. Wang, *Chem. Mater.* **27**, 2495 (2015).
- [47] Y. Hu, X. Zheng, G. Ma, H. Lu, L. Zhang, C. Zhang, Y. Xia, Y. Hao, L. He, J. Chen, F. Shen, S. Wang, C. Wang, D. Wang, and Y. Du, *Phys. Rev. Appl.* **12**, 034027 (2019).

- [48] Y. Song, J. Chen, X. Liu, C. Wang, J. Zhang, H. Liu, H. Zhu, L. Hu, K. Lin, S. Zhang, and X. Xing, *J. Am. Chem. Soc.* **140**, 602 (2018).
- [49] J. Hu, K. Lin, Y. Cao, C. Yu, W. Li, R. Huang, H. E. Fischer, K. Kato, Y. Song, J. Chen, H. Zhang, and X. Xing, *Inorg. Chem.* **58**, 5401 (2019).
- [50] J. Chen, L. Hu, J. Deng, and X. Xing, *Chem. Soc. Rev.* **44**, 3522 (2015).
- [51] G. D. Barrera, J. A. O. Bruno, T. H. K. Barron, and N. L. Allan, *J. Phys.: Condens. Matter* **17**, R217 (2005).
- [52] A. D. Fortes, I. G. Wood, J. P. Brodholt, M. Alfredsson, L. Vočadlo, G. S. McGrady, and K. S. Knight, *J. Chem. Phys.* **119**, 10806 (2003).
- [53] S. Lee, S. Choi, J. Kim, H. Sim, C. Won, S. Lee, S. A. Kim, N. Hur, and J.-G. Park, *J. Phys.: Condens. Matter* **24**, 456004 (2012).